DYNAMICS AND KINEMATICS OF THE ASIAN AND NORTH AMERICAN MONSOON

ANTICYCLONES

A Dissertation

by

LEONG WAI SIU

Submitted to the Office of Graduate and Professional Studies of
Texas A&M University
in partial fulfillment of the requirements for the degree of

DOCTOR OF PHILOSOPHY

Chair of Committee,	Kenneth P. Bowman
Committee Members,	Ping Chang
	Andrew E. Dessler
	Ramalingam Saravanan
Head of Department,	Ramalingam Saravanan

May 2020

Major Subject: Atmospheric Sciences

ABSTRACT

During the boreal warm season (May through September), the circulation in the upper tropo-sphere and lower stratosphere is dominated by two large anticyclones: the Asian monsoon anticy-clone (AMA) and North American monsoon anticyclone (NAMA). Due to variations in the diabatic heating, interactions with Rossby waves propagating along the subtropical jet, and internal dynam-ics within the anticyclone, the circulation of the AMA is unsteady. Here we use the ERA-Interim Reanalysis and trajectories computed with ERA-Interim winds to show that a single circulation center is present only 23% of the time, while two or three sub-vortices are simultaneously present 69% of the time. More than three simultaneous sub-vortices are uncommon. Observed behaviors of the regional sub-vortices include (1) splitting of a single vortex into two vortices; (2) merger of two vortices into a single vortex; (3) vortex shedding in the eastward direction; (4) vortex shedding in the westward direction; and (5) formation, movement, and dissipation of a vortex. The transi-tions between different states of sub-vortices are associated with the appearance and disappearance of hyperbolic regions between the sub-vortices.

The existence of the AMA has long been linked to Asian monsoon precipitation using the Matsuno–Gill framework, but the origin of the NAMA has not been clearly understood. Here the forcing mechanisms of the NAMA are investigated using a simplified dry general circulation model. The simulated anticyclones are in good agreement with observations when the model is forced by a zonally-symmetric meridional temperature gradient plus a realistic geographical distri-bution of heating based on observed tropical and subtropical precipitation in the Northern Hemi-sphere. Model experiments show that the AMA and NAMA are largely independent of one another, and the NAMA is not a downstream response to the Asian monsoon. The primary forcing of the NAMA is precipitation in the longitude sector between $60°$ and $120°$W, with the largest contribu-tion coming from the subtropical latitudes within that sector. Experiments with idealized regional heating distributions reveal that the extratropical response to tropical and subtropical precipitation depends approximately linearly on the magnitude of the forcing, but nonlinearly on its latitude.

The AMA is stronger than the NAMA primarily because precipitation in the subtropics over Asia is much heavier than at similar latitudes in the Western Hemisphere.

DEDICATION

To my Chinese Language and Culture teacher, Mr. Wai Ting Leung (1945–2012).

ACKNOWLEDGEMENTS

CONTRIBUTORS AND FUNDING SOURCES

Contributors

This work was supported by a dissertation committee consisting of Kenneth P. Bowman (advisor), Andrew E. Dessler, and Ramalingam Saravanan of the Department of Atmospheric Sciences and Ping Chang of the Department of Oceanography. The version of the Community Atmosphere Model (CAM) 5.4 in this study was made available through the Simpler Models Initiative as part of the Community Earth System Model (CESM) project; this initiative is supported by National Center for Atmospheric Research (NCAR) under the sponsorship of the National Science Foundation (NSF) and the United States Department of Energy (DOE). The European Centre for Medium-Range Weather Forecasts (ECMWF) produced the ERA-Interim reanalysis product and the NCAR Research Data Archive (RDA) made the data available. The National Aeronautics and Space Administration (NASA) produced the Tropical Rainfall Measuring Mission (TRMM) Multi-satellite Precipitation Analysis (TMPA) product and the NASA Goddard Earth Sciences (GES) Data and Information Services Center (DISC) made the data available.

All work conducted for the dissertation was completed by the student independently. Part of this dissertation is an edited version of the following journal article:

Siu, L. W. and K. P. Bowman, 2019: Forcing of the Upper-Tropospheric Monsoon Anticyclones. J. Atmos. Sci., 76, 1937–1954, https://doi.org/10.1175/JAS-D-18-0340.1 ©American Meteorological Society. Used with permission.

TABLE OF CONTENTS

viii

LIST OF FIGURES

FIGURE
Page

LIST OF TABLES

1.   INTRODUCTION[1]

Traditionally, monsoon refers to the seasonal reversal of the prevailing surface winds in the tropics (Gadgil, 2003). Monsoon regions are distinct from the mid-latitude and polar regions by having two seasons, one dry and the other wet. The winter season is characterized by cool and dry air blowing from the continent, while during boreal summer, the geographical distribution of land and ocean, the pattern of land and sea surface temperature (SST), and the locations of topographic features contribute to driving regional patterns of intense precipitation over southern and eastern Asia and the surrounding oceans.

Figure 1.1a shows the climatological precipitation rate for July, as estimated by the Tropical Rainfall Measuring Mission (TRMM) Multi-satellite Precipitation Analysis (TMPA) (Huffman et al., 2007). In the Eastern Hemisphere, three major precipitation centers are associated with the Asian monsoon: over the west coast of India, the eastern Bay of Bengal, and the Philippines. Smaller regions of intense precipitation are also found in southeast Asia and along the southern margin of the Himalayan front. Less intense precipitation covers a large area over the western Pacific warm pool that lies at the western end of the Intertropical Convergence Zone (ITCZ). This area extends southeastward across the equator and connects with the South Pacific Convergence Zone (SPCZ).

The enormous amount of latent heat released by monsoon precipitation accounts for a large fraction of the total diabatic heating in the tropics (Yanai et al., 1973). This latent heating is important for driving mesoscale convective systems as well as large-scale tropical circulations (Gill, 1982; Holton, 2004). The regional precipitation patterns drive two large-scale anticyclonic circulations (Figure 1.1) in the upper troposphere and lower stratosphere (UTLS), namely the Asian monsoon anticyclone (AMA) and the North American monsoon anticyclone (NAMA). The AMA is centered at $\sim$70°E and $\sim$30°N, also known as the South Asian High (SAH) or the Tibetan anticyclone in the
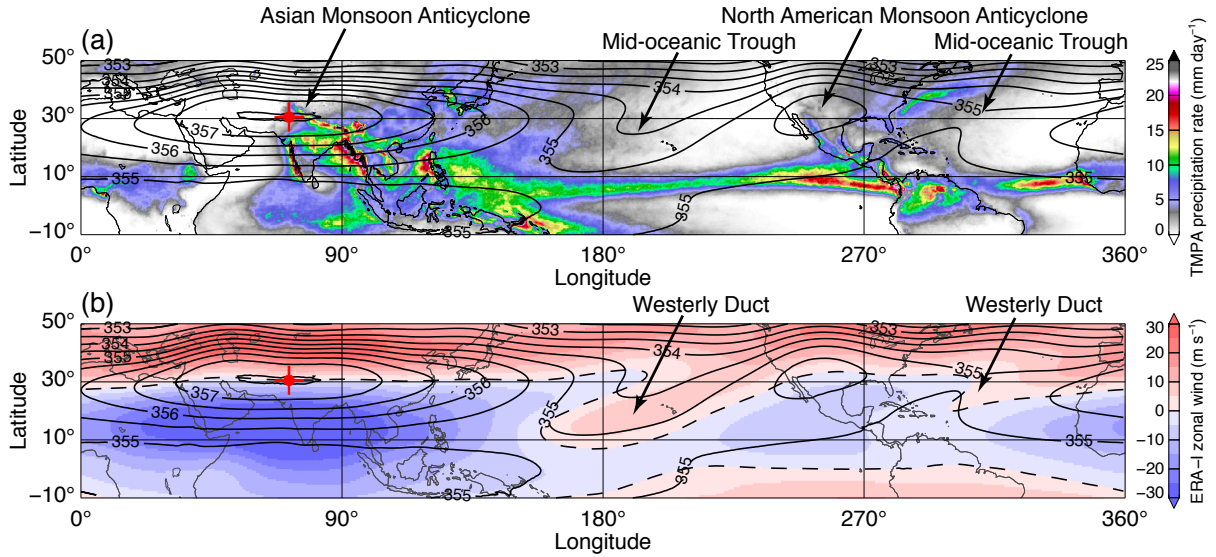
Figure 1.1: (a) TMPA July climatological precipitation rate (color). (b) ERA-Interim July climatological zonal wind u at 370 K (red: $u > 0$; blue: $u < 0$; dashed line: $u = 0$; interval: 5 m s^{-1}). (a)–(b) ERA-Interim July climatological Montgomery streamfunction Ψ at 370 K (solid contours; interval: 0.5 kJ kg^{-1}). The location of the global maximum Ψ along the zero-wind lines ($u = 0$) is indicated by red crosshairs. Climatological positions of the Asian and North American monsoon anticyclones, mid-oceanic troughs, and westerly ducts are labeled and indicated by arrows.

literature. The AMA circulation is flanked by the tropical easterly jet to the south and the subtropical westerly jet to the north (Figure 1.1b). The NAMA, also known as the Mexican High, is located near 110°W and 30°N, but the circulation is not as strong and persistent as its Asian counterpart (Dunkerton, 1995; Chen, 2003; Siu and Bowman, 2019). The NAMA emerges in late May off the Pacific coast of Central America, near the eastern Pacific ITCZ. It then moves northward along the Pacific coast of Mexico until it is centered near northwestern Mexico and the southwestern United States (Douglas et al., 1993). The circulation enters its mature phase in July and August and gradually decays from late September (Vera et al., 2006). Two mid-oceanic troughs over the Pacific and the Atlantic (Figure 1.1a), which are associated with the westerly ducts (Figure 1.1b), separate these two anticyclones (Krishnamurti, 1971; Webster and Holton, 1982).

The discovery of the monsoon anticyclones is closely related to the development of upper-air observations. Some early studies (e.g., Flohn, 1950; Dao and Chen, 1957; Koteswaram, 1958) no-

ticed a high pressure system in the middle and upper troposphere above the Tibetan Plateau from scanty aerological data. Additional research was catalyzed by the International Geophysical Year (IGY) of 1957–58. The World Meteorological Organization (WMO) made considerable efforts during the IGY to expand the global radiosonde network, standardize the observation times, and improve the data quality with better sounding techniques (van Mieghem, 1956). The existence of the AMA was first verified through synoptic upper-air weather maps compiled from the IGY radiosonde data (Koteswaram and Rao, 1963; Mason and Anderson, 1963; Rangarajan, 1963). Since then, the AMA has been regarded as an integral component of the Asian summer monsoon system (Krishnamurti and Bhalme, 1976). Apart from routine radiosonde launches and satellite measurements (e.g., Santee et al., 2017; Luo et al., 2018), the structure and composition of the AMA have recently been investigated by several field campaigns (e.g., Baker et al., 2011; Brunamonti et al., 2018; Gottschaldt et al., 2018; Vernier et al., 2018).

The AMA circulation can be identified on a map by closed contours of high values of Montgomery streamfunction Ψ (contours in Figure 1.1), high geopotential height, or low potential vorticity (PV). The AMA exhibits space-time variations but our current understanding of the underlying mechanisms is rather limited (Randel and Jensen, 2013). Figure 1.2 shows the seasonal evolution of the climatological Montgomery streamfunction Ψ in the Eastern Hemisphere (Hovmöller, 1949). A 32-day ideal low pass Fourier filter has been applied to the original 6-hourly time series and a smaller contour interval (0.1 kJ kg^{-1}) is chosen for $\Psi > 357 \text{ kJ kg}^{-1}$.

The AMA circulation emerges in May and dissipates in September, persisting throughout most of the warm season. The location of the maximum of Ψ (red line) shows that in general the circulation center lies between $\sim 60°$ and $\sim 100°$E. While the variation of Ψ is small near the maximum of Ψ in July and early August, there are two little peaks located at different longitudes. It results in a sharp jump on the location of the maximum of Ψ even all synoptic time scale variabilities have been filtered out. On the other hand, early studies noticed a zonal movement of the AMA on synoptic maps and termed it as the east–west oscillation (e.g., Mason and Anderson, 1963; Dao and Chu, 1964). Using a pentad-mean reanalysis dataset, Zhang et al. (2002) first suggested that the
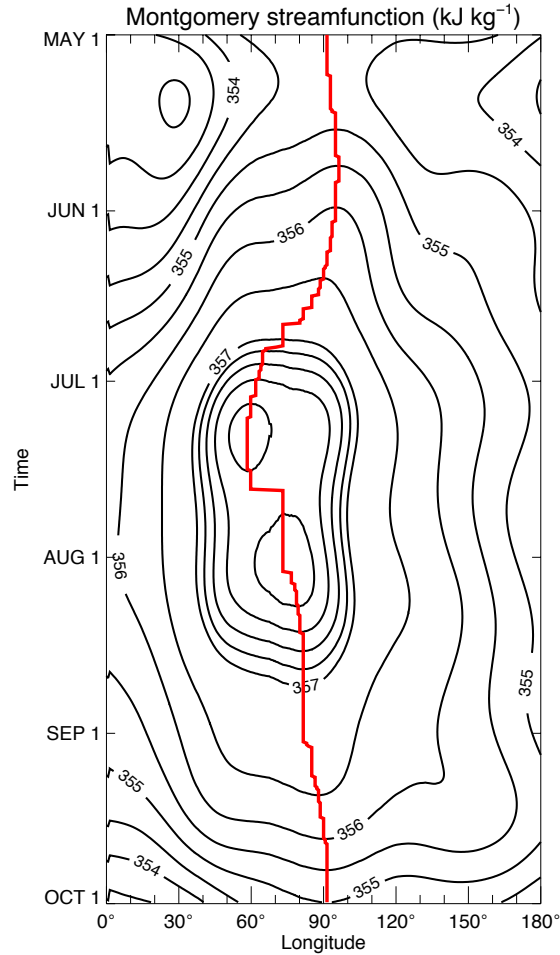
Figure 1.2: Hovmöller plot of ERA-Interim climatological Montgomery streamfunction Ψ (contours; interval: 0.5 kJ kg^{-1} for $\Psi \leq 357$ kJ kg^{-1} and 0.1 kJ kg^{-1} for $\Psi > 357$ kJ kg^{-1}). The original time series at each longitude is the latitudinal averages of Ψ between 25° and 35°N. A 32-day ideal low pass Fourier filter has been applied to smooth the time series. The red dashed line indicates the time series of the maximum Ψ. A similar plot for the year of 2017 is plotted in Figure 5.1.

longitudinal distribution of the AMA is bimodal. That is, the AMA has two preferred circulation center locations, one above the Tibetan Plateau ($\sim 90°$E) and one over Iran ($\sim 60°$E), which are referred to as the Tibetan High and Iranian High, respectively.

   This bimodality can be misleading, however, due to the method used in Zhang et al. (2002) to locate the vortex center, which involves two steps. First, at a specified vertical level the boundary between the tropical easterlies and subtropical westerlies is identified (i.e., the zero-wind line where

zonal wind velocity $u = 0$). Then, the AMA center is defined as the location along this line with maximum geopotential height on a pressure surface (or maximum Ψ on an isentropic surface). That is, only one center is selected at each analysis time (referred to as the single-center method). See Nützel et al. (2016) for a detailed review on this method. Examples of the zero-wind lines (thick black contours) and the AMA center (red crosshairs) based on this single-center approach are shown in Figure 1.1b on the climatological 370 K isentropic surface. In time-averaged flow such as that in Figure 1.1b, the zero-wind line is nearly zonal inside the AMA and the flow field in general is quite smooth. In instantaneous analyses, however, the flow field may be more complex; and several zero-wind lines may appear. As will be demonstrated later, smaller-scale anticyclonic circulations, referred to as sub-vortices, exist intermittently within the larger persistent vortex (Dunkerton, 1995; Dethof et al., 1999).

Zhang et al. (2002) emphasized the different time scales between the bimodal distribution and the east-west oscillations. Several studies have inspected the longitudinal distribution of the AMA center at other time scales. Most find that bimodality exists at time scales longer than 5 days (e.g., Wei et al., 2014) but some report mixed results at shorter time scales. For example, Nützel et al. (2016) examined seven reanalysis datasets using the same method and found that only two of them clearly show a bimodal distribution for daily data at 100 hPa. Garny and Randel (2013) analyzed the distribution of low PV area from a 5-year daily reanalysis dataset but did not see a bimodal distribution at 360 K.

The single-center method is also at odds with some observed transient behavior. Eddy-shedding episodes in the AMA have been documented in several observational studies (e.g., Hsu and Plumb, 2000; Popovic and Plumb, 2001; Vogel et al., 2014; Ploeger et al., 2015; Ungermann et al., 2016; Vogel et al., 2016; Fadnavis et al., 2018). Hsu and Plumb (2000) showed that by imposing sufficient asymmetries in a shallow water model, an anticyclonic vortex could become unstable, split, and shed eddies from the main vortex. By its nature, the single-center method is unable to detect this kind of behavior. The first focus of this study is to characterize the spatiotemporal variations of the AMA circulation and reconcile the disagreement on the existence of a bimodal distribution. We
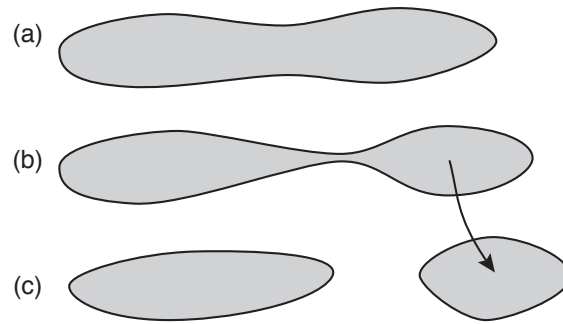
Figure 1.3: Schematic of one possible mode by which fluid is expelled from the anticyclone through 'pinching-off' a compact mass of fluid. The arrow between (b) and (c) indicates the source of the fluid in the detached blob of fluid moving to the right.

find that multiple persistent anticyclonic sub-vortices are present within the AMA a majority of the time.

Understanding the transient behavior of the AMA is important because of its potential impact on the composition of the UTLS (Holton et al., 1995; Dethof et al., 1999). Coupled with deep convection, boundary layer pollutants can be effectively transported into the UTLS (Randel and Park, 2006; Bergman et al., 2013). Once within the AMA, these trace gases may be confined inside the anticyclonic circulation (Ploeger et al., 2015), but mass and trace gas exchange between the upper troposphere and lower stratosphere can occur along isentropic surfaces (Chen, 1995; Dethof et al., 1999; Homeyer et al., 2011; Homeyer and Bowman, 2013). The fluid within the AMA may also be exported via eddy shedding. The second focus of this study is on the transport of fluid in and around the AMA and the role that sub-vortices within the AMA play in transport and stirring. Examples of several types of vortex behavior are shown. Examination of Eulerian maps of quantities such as Ψ and PV frequently gives the impression that eddy shedding operates through a pinching-off process, illustrated schematically in Figure 1.3, where the interior of the anticyclone is shown in gray. Through the use of Lagrangian diagnostics, we will show that in the case of the AMA, eddy shedding actually happens through stretching and folding associated with regions of hyperbolic flow that exist between two sub-vortices within the overall AMA circulation.

The AMA has long been viewed as, to first order, a response to the latent heat of condensation released by tropical and subtropical precipitation in the Eastern Hemisphere (e.g., Webster, 1972; Gill, 1980; Phlips and Gill, 1987; Hoskins and Rodwell, 1995; Highwood and Hoskins, 1998). Gill (1980) extended the study of Matsuno (1966) and investigated the steady-state response of the linearized shallow water equations on an equatorial β-plane in a resting atmosphere forced by simple heating distributions. The upper-tropospheric AMA can be considered as a westward-propagating Rossby wave response to tropical heat sources. To the east of the heat sources, an eastward-propagating Kelvin wave response is also excited. The strength of the steady-state Rossby wave response is governed by the linear inviscid vorticity equation or so-called the Sverdrup balance (Vallis, 2017), which can be written as

$$\beta v = -f(\nabla \cdot \mathbf{v}), \tag{1.1}$$

where $\mathbf{v} = (u, v)$ is the horizontal wind velocity vector; f is the Coriolis parameter; $\beta = \partial f / \partial y$ is the meridional gradient of f at a given latitude. Note that the strength of the Gill-type response (1.1) is proportional to both the Coriolis parameter f, which is a function of latitude, and the divergence of the horizontal wind $\nabla \cdot \mathbf{v}$, which is proportional to the magnitude of the heating. Schumacher et al. (2004) simulated a reasonable quasi-steady-state response of the AMA at 250 hPa using a simplified general circulation model (GCM) forced by a TMPA-derived three-dimensional latent heating distribution. The Gill-type response was also used to explain the existence of the upper-tropospheric anticyclones over northwestern Australia during the *El Niño Modoki* events (Taschetto et al., 2010) and over west-central South America during the austral warm season (Lenters and Cook, 1997).

The origin of the upper-tropospheric NAMA circulation, however, is not clear. There are a number of studies on the spatial and temporal variations of precipitation in the North American monsoon (NAM) region, including Mexico and the United States (e.g., Douglas et al., 1993; Adams and Comrie, 1997; Barlow et al., 1998; Higgins et al., 1997, 1998, 1999). Higgins et al. (1997,

1998) showed that during July and August the strength of the NAMA is related to the amount of precipitation in Arizona and New Mexico. Stensrud (2013) demonstrated the importance of diabatic heating in simulating the NAMA using a mesoscale numerical model. Chao and Chen (2001) asserted that land-sea contrasts and orography are important for simulating the North American monsoon. Other thermal forcings may also be important. The heaviest North American monsoon precipitation is located along the Sierra Madre Occidental in northwestern Mexico; however, the heaviest precipitation in the Western Hemisphere falls in the equatorial Pacific and Atlantic ITCZs, Central America, and the northern part of South America (Figure 1.1a). Given its magnitude and proximity, the ITCZ precipitation may contribute to the formation of the NAMA. In addition, heat sources in the Asia monsoon region may play a role through downstream wave effects. Chen et al. (2001) showed that in a linear, quasi-geostrophic model the subtropical anticyclones in the lower troposphere over the North Pacific and the North Atlantic are a remote response to the Asian heat sources. Jiang and Lau (2008) showed that intra-seasonal variability of the North American monsoon is associated with convective activity in the subtropical western North Pacific via a trans-Pacific wave train.

The fundamental dynamics of the NAMA may be a Matsuno–Gill type response, but much is not understood about the origin and dynamics of the anticyclone and the contributions of heating from different regions. The third focus of this study is to investigate whether the NAMA is a response to the diabatic heating from the Asian monsoon region, the North American monsoon region, the ITCZ, or a combination thereof. Our approach is through running numerical experiments with a simplified dry GCM dynamical core forced by observed and idealized heating distributions.

2.   DATA[1]

2.1   ERA-Interim Reanalysis

The primary data source for this study is the ERA-Interim (ERA-I) reanalysis, which is produced by the European Centre for Medium-Range Weather Forecasts (ECMWF) (Dee et al., 2011). We use 39 years (1979–2017) of the ERA-I analyses obtained from the National Center for Atmospheric Research (NCAR) Research Data Archive (RDA) (ECMWF, 2009). Analyses are available at 6-hour intervals (00, 06, 12, and 18 UTC) on the N128 global reduced-Gaussian grid with a latitude-longitude grid spacing of $\sim0.7° \times \sim0.7°$ (~80 km $\times \sim80$ km).

To provide an observational foundation for the numerical experiments, we use ERA-I variables that have been interpolated from the original 60-level η-coordinate model grid to 37 unevenly-spaced pressure levels. The topmost pressure level is 1 hPa. To characterize the observed behavior of the monsoon anticyclones, we also use variables on 15 irregularly-spaced isentropic surfaces from 265 to 850 K. Monthly averages are computed as a simple arithmetic average of the 6-hourly data for the period of 1979 to 2017. Climatological monthly averages are computed in a similar method from the monthly averages.

2.2   TRMM Multi-satellite Precipitation Analysis

Precipitation estimates come from version 7 of the TRMM Multi-satellite Precipitation Analysis (TMPA) (Huffman et al., 2007; Huffman and Bolvin, 2018). This analysis is also referred to as the 3B42 product. To prescribe the horizontal latent heating distribution, which is used to specify diabatic heating rates in the GCM, we use 19 years (1998–2016) of TMPA obtained from the National Aeronautics and Space Administration (NASA) Precipitation Measurement Missions (PMM) data archive (TRMM, 2011).

The TMPA is based primarily on measurements from microwave imaging radiometers on mul-

---

[1]Part of this chapter is reprinted with permission from 'Forcing of the Upper-Tropospheric Monsoon Anticyclones.' by L. W. Siu and K. P. Bowman, 2019. J. Atmos. Sci., 76, 1937–1954, Copyright 2019 by American Meteorological Society.

tiple satellites. The TMPA data cover the latitude zone from 50°S to 50°N. Data consist of area-averaged precipitation rates for 0.25° × 0.25° longitude-latitude grid boxes at 3-hour intervals centered on the nominal observing times of 00, 03, …, 21 UTC. Within each 3-hour window, if observations are available for a grid box from multiple microwave instruments, the values are averaged using simple arithmetic averaging. Monthly and climatological averages are computed in a similar method from the 3-hourly data and monthly averages, respectively.

3. METHODS

3.1 Eulerian Methods

Here we present an improved method based on Zhang et al. (2002) to identify and track multiple monsoon sub-vortices in three steps. This is referred to as the multiple-center method. The ERA-I variables used to locate vortices include the Montgomery streamfunction Ψ, zonal wind u, and relative vorticity ζ.

3.1.1 Marching Squares Algorithm

The first step is to identify zonal zero-wind lines for the specified domain at a given analysis time. While numerical analysis software packages generally include procedures for contouring gridded data, the underlying algorithms vary and can give different results for the same input data. To ensure the replicability of this study (Irving, 2016), we implement the marching squares algorithm to find isopleths of $u = 0$ (Rajon and Bolch, 2003; Mantz et al., 2008). This algorithm is the two-dimensional analog of the original marching cubes algorithm used to find three-dimensional isosurfaces (Lorensen and Cline, 1987).

A family of variants has been proposed to improve the algorithm since its introduction. In this study we mainly follow the method outlined in Mantz et al. (2008). In brief, the algorithm first partitions the instantaneous two-dimensional zonal wind field u into multiple marching squares (each with 2×2 grid points) and then uses a divide-and-conquer approach to find the intersection points of a selected value (in this case $u = 0$) for each marching square. Multiple distinct isopleths may be extracted by connecting these intersection points. Isopleths either end at the boundary of the domain or close upon themselves. The algorithm can be implemented in a simple and efficient manner using common programming languages. The output of the algorithm is a set of n continuous piecewise-linear two-dimensional curves (contours) identified by subscript j, where $j = 1, \ldots, n$. For a contour having m segments and $m + 1$ nodes, the coordinates (x_i, y_i) of the endpoints of the segments are identified by subscript i, where $i = 0, \ldots, m$. Note that by the nature of the algorithm,

all endpoints (x_i, y_i) lie along the meridians or parallels that define the original ERA-I grid.

3.1.2 Vortex Identification

After extracting one or more zero-wind lines u_j within the analysis domain, the second step is to identify vortex centers (if any) along the zero-wind lines and filter out spurious vortices that may arise from small-scale noise in the gridded data. For vortex identification, the Montgomery streamfunction Ψ is interpolated to each node (x_i, y_i) on the jth contour of u_j to give Ψ_j. Often it is convenient to represent $\Psi_j(x_i, y_i)$ as $\Psi_j(s_i)$, where s_i is the contour length from its starting point (x_0, y_0). The value of s_i is computed as the sum of the great-circle lengths of the contour segments between (x_0, y_0) and (x_i, y_i).

For each contour the one-dimensional function $\Psi_j(s_i)$ is searched to locate local maxima. A local maximum is identified at $s_k = (x_k, y_k)$ if $\Psi_j(s_k)$ is the largest value within the range $s_k - \delta s \leq s_k \leq s_k + \delta s$, where δs is the half width of the search window. Here the half-width δs is set to 7.5° of great-circle arc. This value is chosen through sensitivity testing to be as small as possible while excluding vortices that are much smaller than the Rossby radius of deformation. Therefore, in order to be searched, the length of the contour must be at least $2 \times \delta s = 15°$. Because of the half-width requirement, it is necessary to choose a reasonably large domain to avoid edge effects. This approach has the following properties: along a contour the minimum possible separation between identified peaks (vortex centers) is δs, and the number of distinct vortices identified may vary with time.

Two criteria to filter out spurious peaks are shown schematically in Figure 3.1. For each identified peak at (x_k, y_k), the closest ERA-I grid point is located and defined as the central grid point (black dot). Note that since all vortex centers are either along the meridians or parallels of the ERA-I grid, the maximum distance between the vortex center and the ERA-I central grid point is $\sim 0.35°$.

The first criterion requires that the relative vorticity ζ of the central grid point (black dot) and its four nearest neighbors (black crosses) must be anticyclonic ($\zeta < 0$ in the Northern Hemisphere

12
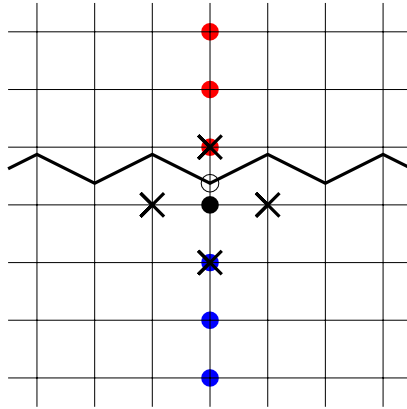
Figure 3.1: Illustration of the criteria of filtering spurious vortex centers found by the marching square algorithm. A vortex center (open circle) is located along a zero-wind line (thick black line). The closest ERA-Interim grid point to this vortex center is indicated by the black dot. The first criterion requires that the relative vorticity ζ at this grid point (black dot) and its four nearest neighbors (black crosses) are anticyclonic ($\zeta < 0$ in the Northern Hemisphere and $\zeta > 0$ in the Southern Hemisphere). The second criterion requires that the three grid points poleward (equatorward) of this closest grid point must be westerlies (easterlies), which are indicated by red (blue) dots. The second criterion is inverted in latitude when applied in the Southern Hemisphere.

or $\zeta > 0$ in the Southern Hemisphere). Note that some studies have used the meridional gradient of zonal wind $\partial u/\partial y$ (e.g., Zarrin et al., 2010), which ignores the contribution of the zonal gradient of meridional wind $\partial v/\partial x$ to the relative vorticity. The second criterion considers the zonal wind field along the same meridian of the central grid point, which requires that three nearest grid points poleward and equatorward of the central grid point must be westerlies ($u > 0$) and easterlies ($u < 0$), respectively.

To illustrate, Figure 3.2a shows the ERA-I zonal wind u and Montgomery streamfunction Ψ on the 370 K isentropic surface for 00 UTC on 19 August 2017. Blue and red colors indicate easterlies and westerlies, respectively. Dashed contours (black in Figure 3.2a and yellow in Figure 3.2b) indicate three zero-wind lines found by the marching squares algorithm. Figure 3.2c shows the Montgomery streanfunction along the zero-wind lines $\Psi_j(s_i)$ as a function of longitude. Three
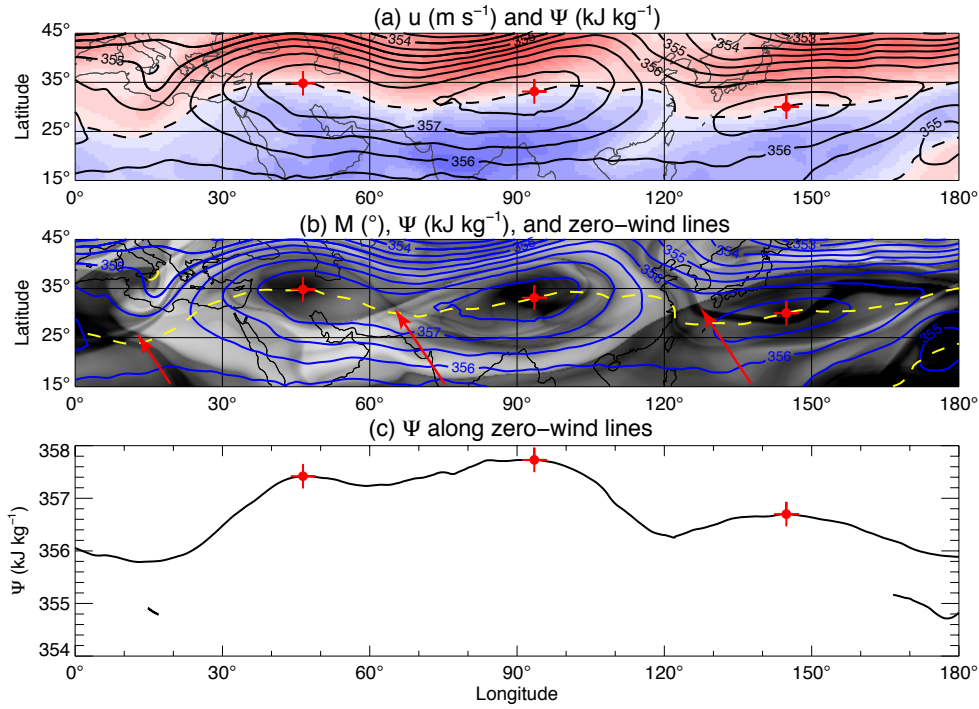
Figure 3.2: Illustration of the method used to identify vortices within the Asian monsoon anticyclone. Data are for 2017-08-19 00 UTC at 370 K. (a) Zonal wind u (red: $u > 0$; blue: $u < 0$; dashed line: $u = 0$; interval: 5 m s^{-1}) and Montgomery streamfunction Ψ (contours; interval: 0.5 kJ kg^{-1}). (b) M for $\tau = 5$ days (grayscale), Ψ (blue contours; interval: 0.5 kJ kg^{-1}), and zero-wind lines $u = 0$ (yellow dashed). Large and small M values are light and dark, respectively. Some hyperbolic regions are indicated by red arrows. (c) Ψ along zero-wind lines as a function of longitude. (a)–(c) Locations of local maxima in Ψ are indicated by red crosshairs identified by the method described in chapter 3.

identified vortex centers are located near 45°E, 90°E, and 150°E, respectively. All these centers fulfill the two filtering criteria and are indicated by red crosshairs in all three panels of Figure 3.2. For the closed contour near 15°E, no peak is identified because the length of the contour is less than 15°. For the contour near 170°E, no peak is identified because easterlies are located on the poleward side of the contour.

3.1.3 Vortex Tracking

The final step is to track the persistence and movement of sub-vortices through time by repeating the vortex analysis at a sequence of analysis times. Vortices are defined to be persistent if, from

14

one time step to the next, the location of a vortex does not change by more than 10° of great-circle distance, and a vortex is continuous for at least four analysis periods (18 hours). The remaining vortices are defined to be transient. As will be shown, by applying these definitions it is relatively easy to track vortex motion and to identify possible vortex splitting, merger, and dissolution.

3.2 Lagrangian Methods

3.2.1 Trajectories

Fluid motion within and around the AMA is diagnosed kinematically using particle trajectories. Particles are assumed to represent hypothetical massless air parcels. Trajectories are computed numerically using the TRAJ3D trajectory model (Bowman, 1993; Bowman and Carrie, 2002) to solve the kinematic equations of motion

$$\frac{d\mathbf{x}(t)}{dt} = \mathbf{v}(\mathbf{x}(t), t), \tag{3.1}$$

where $\mathbf{x}(t)$ is the particle position of as a function of time t, and $\mathbf{v}(\mathbf{x}, t)$ is the particle velocity as a function of particle position $\mathbf{x}$ and time t. Trajectory calculations use the isentropic-coordinate version of the ERA-Interim reanalysis data and the flow field is linearly interpolated in space and time to particle locations. Trajectories are computed using a fourth-order Runge–Kutta scheme with a time step of 45 minutes (32 time steps per day). Since heating rates are small in this part of the atmosphere, the motion can be assumed to be adiabatic to a good approximation for the time scales examined here. Hence the vertical velocity $d\theta/dt$ is set to zero.

3.2.2 M Diagnostics

Stirring of fluid in and around the AMA is evaluated qualitatively using the M diagnostic devised by Madrid and Mancho (2009). The quantity M is defined as follows:

$$M(\mathbf{x}_0, t_0, \tau) = \int_{t_0-\tau}^{t_0+\tau} |\mathbf{v}(\mathbf{x}(t_0), t)| \, dt, \tag{3.2}$$

where $\mathbf{x}_0$ is the particle position $\mathbf{x}$ along the trajectory at time t_0, $|\mathbf{v}|$ is the speed of the particle, and $\tau > 0$. That is, M is the length of the trajectory beginning at $t_0 - \tau$ and ending at $t_0 + \tau$ that passes through $\mathbf{x}_0$ at time t_0. In practice M is computed by adding the lengths of forward and backward trajectories initialized at location $\mathbf{x}_0$ at time t_0 for periods of $-\tau$ and $+\tau$. Examples of geophysical applications of M such as transport in the Antarctic circumpolar vortex can be found in de la Cámara et al. (2012) and de la Cámara et al. (2013).

Figure 3.2b shows the corresponding M field in the example of vortex identification discussed in chapter 3.1. An initial grid of particles with a horizontal spacing of $0.25° \times 0.25°$ (1440×321 particles) is integrated forward and backward from the reference time for 15 days. In this example M is computed using $\tau = 5$ days, so M represents the length of 10-day trajectories. Large values of M, which represent long particle trajectories, are shown as light shades of gray. Small values of M are dark. The instantaneous Montgomery streamfunction Ψ is overplotted in blue. Red crosshairs show the centers of the sub-vortices within the main anticyclone and red arrows indicate the locations of prominent hyperbolic regions in the flow field associated with the AMA. Hyperbolic regions play a crucial role in fluid transport and stirring (Wiggins, 1992).

The importance of hyperbolic regions in stirring is illustrated in Figure 1 of de la Cámara et al. (2013). (Here we use *stirring* to mean the creation of fine structure in fluid tracers by the resolved flow, which may in fact be quite smooth, and *mixing* to mean the mixing of fluid at the molecular level.) If the flow field is steady, streamlines are also material lines and there is shearing of the fluid, but no stirring (panel A). In this case the heavy streamlines divide the fluid into parts that are inside and outside the vortices, and there is no exchange of fluid across those streamlines. Hyperbolic points exist and trajectories near hyperbolic points have the following behavior: A fluid parcel moves toward a hyperbolic point along a material line (stable manifold) and is pulled away from a hyperbolic point along an orthogonal material line (unstable manifold). When the flow is time dependent, however, the streamlines move relative to material lines in the fluid. Fluid that was inside the vortex may find itself outside, and vice versa (panel B). Patches of fluid exchanged across the nominal vortex boundaries are referred to as lobes (panel C).

In unsteady flows hyperbolic regions can be identified as regions with intersecting boundaries between regions with similar values of M (Figure 3.2b). The flow in a hyperbolic region can rapidly collapse filaments of fluid into compact patches and then stretch those compact patches into narrow filaments. The overlapping tangle of these patches, which characterizes time dependent flow in a hyperbolic region, produces a chaotic layer around the vortices where fluid is continually exchanged between the interior and exterior of the vortices by the collapse or creation of filaments. Examples will be given below.

Figure 3.2b reveals a relationship between the M field and the instantaneous Montgomery streamfunction Ψ, although the relationship is not one-to-one or monotonic. The largest values of M (i.e., the largest average Lagrangian speeds and longest particle trajectories) lie in a ring around the AMA. Intermediate values of M lie largely in the subtropical jet, while in the tropics weak easterlies lead to short trajectories. Air is at least partially confined within the AMA, as the small values of M within the two sub-vortices show. The principal hyperbolic regions in the flow associated with the AMA are identified by red arrows. The layering of the M field in these regions indicates the boundaries of the lobes. These often occur near saddle points in Ψ, where the instantaneous flow is hyperbolic, but this is not always the case, as M integrates the Lagrangian behavior of the fluid over an extended time, during which hyperbolic regions can appear, disappear, or move with the flow.

4.   GENERAL CIRCULATION MODEL[1]

4.1   Dynamical Core

We use the dry Eulerian spectral dynamical core of the NCAR Community Atmosphere Model (CAM), Version 5.4, which is the atmospheric component of the Community Earth System Model (CESM). The dynamical core solves the hydrostatic primitive equations formulated in vorticity-divergence form on a hybrid sigma–pressure (σ–p), or η coordinate, using a spectral transform method in the horizontal, a finite difference method in the vertical, and a semi-implicit leapfrog scheme for time integration (Neale et al., 2012). The model has no topography or moisture. A linear harmonic ∇^2 diffusion is used in the top three model levels to absorb vertically propagating planetary wave energy and a linear biharmonic ∇^4 diffusion is used in all other levels for sub-grid-scale dissipation. Monthly averages and 6-hourly instantaneous model outputs are archived for offline calculations. Model variables are interpolated to the ERA-Interim pressure levels when necessary.

4.2   Idealized Physics Package

One of the goals of Version 2 of the CESM is to support simpler model configurations. As a result, CAM 5.4 offers an idealized physics configuration based on Held and Suarez (1994, hereafter HS94) as an alternative to full physics parameterizations. While the default HS94 simulation resembles the general circulation of the atmosphere in equinoctial conditions, the height of the climatological tropical tropopause differs somewhat from observations (340–350 K versus 360–380 K) and the tropical lapse rate in radiative equilibrium follows the dry adiabatic lapse rate rather than the moist one (Tandon et al., 2011). Since this study is focused on the tropical UTLS region, we adopt an HS94-like physics package from Schneider (2004) and Schneider and Walker (2006, hereafter SW06) to better reproduce the tropical circulation. The two Schneider configurations

---

Table 4.1: Selected parameters of the idealized physics package described in chapter 4. Parameters related to the horizontal distribution of thermal forcing are summarized in Tables 4.2 and 4.3.

Description	Symbol	Value
Average radius of the earth	a	6.37122×10^6 m
Acceleration of gravity	g	9.80616 m s^{-2}
Specific heat of dry air at constant pressure	c_p	1004.64 J kg^{-1} K^{-1}
Latent heat of condensation of water	L_v	2.5×10^6 J kg^{-1}
Density of water	ρ	1000 kg m^{-3}
Frictional wavenumber near the surface	k_d^0	0.7×10^{-5} m^{-1}
Extent of boundary layer	η_{BL}	0.85
Equatorial temperature	$T_{equator}^r$	345 K
Minimum radiative equilibrium temperature	T_{min}^r	200 K
Pole-to-equator temperature difference in equinoctial conditions	Δ_h	30 K
Latitude of maximum surface radiative equilibrium temperature	ϕ_0^r	20°N
Scale height ratio	α	3.5
Radiative relaxation time scale in the free atmosphere	τ_a	55 day
Radiative relaxation time scale near surface	τ_s	7 day
Convective relaxation time scale	τ_c	4 day
Dry adiabatic lapse rate	Γ_d	9.8 K km^{-1}
Rescaling factor of pseudoadiabatic lapse rate	γ	0.85
Reference surface pressure	p_0	1000 hPa
Top pressure level of thermal forcing	p_t	100 hPa
Bottom pressure level of thermal forcing	p_b	1000 hPa
Normalization factor of vertical distribution of thermal forcing	A	1.570247
Shape parameter of vertical distribution of thermal forcing	B	1

differ slightly in their treatment of the moist adiabatic profile; therefore, we make reference only to the SW06 configuration from here on. Values of selected parameters of the idealized physics package are given in Table 4.1.

4.2.1 Surface Drag

A quadratic drag is applied to the horizontal wind within the planetary boundary layer. The depth of the boundary layer extends to $\eta_{BL} = 0.85$. The strength of the drag depends on the frictional wavenumber at the surface k_d^0.

4.2.2 Radiative Processes

Newtonian relaxation is used to represent radiative forcing and moist convection in a semigray atmosphere. Similar to Tandon et al. (2013), the prognostic equation for temperature T is

$$\frac{\partial T}{\partial t} = \cdots - \frac{T - T^r(\phi, p)}{\tau_r(\phi, \eta)} - \frac{T - T^c(\lambda, \phi, p, t)}{\tau_c} + Q_{LH}(\lambda, \phi, p), \tag{4.1}$$

where λ, ϕ, η, p, and t are longitude, latitude, hybrid vertical coordinate, pressure, and time; T^r and τ_r are the radiative equilibrium temperature and relaxation time scale; T^c and τ_c are the convective equilibrium temperature and relaxation time scale; Q_{LH} is the external thermal forcing that represents latent heating.

The radiative heating Q_R is parameterized as the first term on the right-hand side (rhs) of (4.1). First, the surface temperature at radiative equilibrium T_s^r is prescribed as

$$T_s^r(\phi) = T_{equator}^r - \Delta_h(\sin^2 \phi - 2 \sin \phi_0^r \sin \phi), \tag{4.2}$$

where $T_{equator}^r$ is the equatorial temperature; ϕ_0^r is the latitude of maximum surface radiative equilibrium temperature; and Δ_h is the pole-to-equator temperature difference under equinoctial conditions. Note that the form of T_s^r is identical to Schneider and Bordoni (2008) and depends on latitude ϕ only. The optical thickness of the atmosphere at different latitudes is determined by the surface radiative equilibrium temperature T_s^r and the minimum radiative equilibrium temperature at the top of atmosphere T_{min}^r as in SW06. Then the radiative equilibrium temperature T^r can be computed by

$$T^r(\phi, p) = T_{min}^r \left[1 + d_0(\phi) \left(\frac{p}{p_0} \right)^\alpha \right]^{1/4}, \tag{4.3}$$

where $T_{min}^r = 200$ K; $p_0 = 1000$ hPa is the reference surface pressure; d_0 is the optical thickness of the semigray atmosphere; α is the scale height ratio. The radiative equilibrium temperature T^r at 1000 hPa of this form is matched up with the surface radiative equilibrium temperature T_s^r.

The temperature field T is relaxed toward the zonally symmetric radiative equilibrium temper-

ature profile T^r with a radiative time scale τ_r, which depends on both latitude and vertical level as in SW06. In this study, τ_r is equal to $\tau_a = 55$ day in the free atmosphere and decreases linearly within the boundary layer to $\tau_s = 7$ day near the surface.

4.2.3   Convective Adjustment

The convective heating Q_C is parameterized as the second term on the rhs of (4.1) to represent convective adjustment. This term is absent in the original HS94 configuration, in which the adjustment is implicitly done via a judiciously chosen equilibrium radiative temperature profile. The radiative equilibrium temperature of the SW06 configuration, however, is statically unstable for most of the lower troposphere, which necessitates the inclusion of a simple dry convection scheme. This scheme relaxes the temperature field T toward the convective equilibrium temperature T^c on the convective time scale τ_c only when a layer is statically unstable in comparison with the convective lapse rate and has a positive convective available potential energy. The convective lapse rate is $\gamma \, \Gamma_d$, where $\Gamma_d = 9.8$ K km^{-1} is the dry adiabatic lapse rate, and $\gamma = 0.85$ is a nondimensional scale factor to represent the effect of moist convection.

4.2.4   Thermal Forcing

The latent heating Q_{LH} is the last term on the rhs of (4.1). It represents an imposed three-dimensional thermal forcing due to latent heat of condensation, which is expressed as

$$Q_{LH}(\lambda, \phi, p) = Q_0 \times Q_h(\lambda, \phi) \times Q_v(p), \tag{4.4}$$

where Q_0 is a dimensional parameter that determines the magnitude of the thermal forcing; Q_h and Q_v are the horizontal and vertical distributions of the thermal forcing, respectively. Therefore, the unit of Q_0 is K day^{-1}, while Q_h and Q_v are dimensionless. Note that T^r and Q_{LH} have no time dependence in (4.1) and (4.4), respectively; there are, therefore, no diurnal or seasonal cycles.

In this study the horizontal distribution of the thermal forcing Q_h is either derived from the observed TMPA precipitation rate R or specified as idealized distributions. For the former, the

observed precipitation field, given a specified range of longitude and latitude, is first area-averaged from the TMPA grid to the model grid, taking care to preserve the total amount of precipitation. Then Q_h is obtained by normalizing the area-averaged precipitation field.

For the latter, two idealized horizontal precipitation distributions are being used. The first one is a zonally-elongated thermal forcing, which resembles the appearance of the Pacific ITCZ and is specified as

$$Q_h(\lambda, \phi) = \begin{cases} \cos^2\left[\left(\frac{\phi-\phi_0}{\Delta\phi}\right)\pi\right], & \text{if } |\lambda - \lambda_0| \leq \frac{\Delta\lambda}{2}, |\phi - \phi_0| \leq \frac{\Delta\phi}{2}, \\ 0, & \text{elsewhere,} \end{cases} \tag{4.5}$$

where λ_0 and ϕ_0 are the center longitude and latitude of the forcing; $\Delta\lambda$ and $\Delta\phi$ are the zonal and meridional extents of the forcing. Note that within the forcing region the strength of the forcing is uniform in the zonal direction.

The second one is a more compact regional forcing given by

$$Q_h(\lambda, \phi) = \begin{cases} \cos\left[\left(\frac{\lambda-\lambda_0}{\Delta\lambda}\right)\pi\right]\cos^2\left[\left(\frac{\phi-\phi_0}{\Delta\phi}\right)\pi\right], & \text{if } |\lambda - \lambda_0| \leq \frac{\Delta\lambda}{2}, |\phi - \phi_0| \leq \frac{\Delta\phi}{2}, \\ 0, & \text{elsewhere.} \end{cases} \tag{4.6}$$

The vertical distribution of the thermal forcing Q_v is identical to DeMaria (1985), which is prescribed as

$$Q_v(p) = \begin{cases} A\sin\left[\left(\frac{p-p_t}{p_b-p_t}\right)\pi\right]\exp\left[-B\left(\frac{p-p_t}{p_b-p_t}\right)\right], & \text{if } p_t \leq p \leq p_b, \\ 0, & \text{elsewhere,} \end{cases} \tag{4.7}$$

where Q_v is a function of pressure; p_t and p_b are the top and bottom pressure levels of the forcing, respectively; A is a dimensionless factor to normalize the range of Q_v to be between 0 and 1; and B is a constant to change the shape of Q_v. In this study, all numerical experiments use different horizontal distributions of thermal forcing Q_h but the same vertical distribution Q_v.

Table 4.2: Summary of the numerical experiments with thermal forcing based on the TMPA observations. Second column gives the model resolution. Third through fifth columns give the description, latitude range, and longitude range of the forcing, respectively. Last two columns give the maximum magnitude Q_0 and total amount Q_{total} of the forcing, respectively. Information of TMPA observations is included for reference. All experiments use the same vertical distribution of thermal forcing (Table 4.1).

Run	Resolution	Description	Latitude Range	Longitude Range	Q_0	Q_{total}
					(K day^{-1})	(10^{19} J day^{-1})
TMPA	–	Tropics and subtropics	5°S–40°N	180°W–180°E	–	187.95
1a	T42L30	No forcing	–	–	0.00	0.00
1b	T85L30	No forcing	–	–	0.00	0.00
1c	T42L60	No forcing	–	–	0.00	0.00
2a	T42L30	Tropics and subtropics	5°S–40°N	180°W–180°E	6.35	110.16
2b	T42L30	EH tropics and subtropics	5°S–40°N	0°–180°E	6.35	66.66
2c	T42L30	WH tropics and subtropics	5°S–40°N	180°W–0°	4.87	43.50
3a	T42L30	Central Pacific	5°S–40°N	180°–120°W	3.54	10.33
3b	T42L30	NAM region and Eastern Pacific	5°S–40°N	120°–60°W	4.87	21.97
3c	T42L30	Atlantic	5°S–40°N	60°W–0°	4.58	11.20
3d	T42L30	Tropical part of 3a	5°S–15°N	180°–120°W	3.54	8.41
3e	T42L30	Tropical part of 3b	5°S–15°N	120°–60°W	4.87	13.54
3f	T42L30	Tropical part of 3c	5°S–15°N	60°W–0°	4.58	9.45
3g	T42L30	Subtropical part of 3a	15°–40°N	180°–120°W	0.71	1.91
3h	T42L30	Subtropical part of 3b	15°–40°N	120°–60°W	2.81	8.43
3i	T42L30	Subtropical part of 3c	15°–40°N	60°W–0°	1.52	1.75

The forcing magnitude parameter Q_0 is tuned through sensitivity experiments to produce the best possible simulation of the global circulation, with an emphasis on the amplitude and location of the tropical easterlies, subtropical westerlies, and monsoon anticyclones. To facilitate the

comparison of latent heating between TMPA observations and model, we compute the global total latent heating Q_{total} in J day^{-1}. The total amount of latent heating from the observed precipitation rate is given by

$$Q_{total} = \iint \rho \, L_v \, R(\lambda, \phi) \, a^2 \cos \phi \, \mathrm{d}\phi \mathrm{d}\lambda, \qquad (4.8)$$

where ρ is the density of water, L_v is the latent heat of vaporization of water, $R(\lambda, \phi)$ is the two-dimensional TMPA precipitation in m day^{-1}, and a is the average radius of the earth.

Under the hydrostatic assumption, the total amount of latent heating in the model is defined as

$$Q_{total} = \iiint c_p \, Q_{LH}(\lambda, \phi, p) \, a^2 \cos \phi \, \mathrm{d}\phi \mathrm{d}\lambda \frac{\mathrm{d}p}{g}, \qquad (4.9)$$

where c_p is the specific heat of dry air at constant pressure, $Q_{LH}(\lambda, \phi, p)$ is the three-dimensional thermal forcing computed from (4.4), and g is the acceleration of gravity.

4.3 Experimental Design

To evaluate the contribution of latent heating in different parts of the tropics and northern hemisphere subtropics to driving the NAMA, we carry out numerical experiments using the simplified GCM. The parameters of the realistic and idealized heating experiments are summarized in Tables 4.2 and 4.3, respectively. The control experiments (runs 1a–1c) have zero forcing ($Q_0 = 0$ K day^{-1}). The first set of perturbed experiments (runs 2a–2c) uses realistic heating distributions derived from the TMPA climatological July precipitation rate to investigate the contribution of the global and hemispheric heating to driving the NAMA. The second set of perturbed experiments (runs 3a–3i) further analyzes the contribution of different regions in the western hemisphere to the NAMA response. Additional experiments 4 to 6 examine the response to the idealized heating distributions specified by (4.5) and (4.6). The last set of experiment is used to test the model sensitivity to both horizontal resolution (runs 7a–7e) and vertical resolution (runs 7f–7j).

Most of the numerical experiments are integrated for 600 days at T42L30 resolution, denoting a triangular truncation of the spherical harmonic series at wavenumber 42 ($\sim 2.8° \times \sim 2.8°$ in latitude

Table 4.3: Summary of the numerical experiments with idealized zonally-elongated and compact regional thermal forcings. Second column gives the model resolution. Third through seventh columns give the description, center longitude λ_0, zonal extent $\Delta\lambda$, center latitude ϕ_0, and meridional extent $\Delta\phi$ of the forcing, respectively. Last two columns give the maximum magnitude Q_0 and total amount Q_{total} of the forcing, respectively. All experiments use the same vertical distribution of thermal forcing (Table 4.1).

Run	Resolution	Description	λ_0 (°W)	$\Delta\lambda$ (°)	ϕ_0 (°N)	$\Delta\phi$ (°)	Q_0 (K day^{-1})	Q_{total} (10^{19} J day^{-1})
4a	T42L30	zonally-elongated	180	360	0	15	2.41	50.00
4b	T42L30	zonally-elongated	180	360	7.5	15	2.61	50.00
4c	T42L30	zonally-elongated	180	360	15	15	2.69	50.00
4d	T42L30	zonally-elongated	180	360	22.5	15	2.66	50.00
4e	T42L30	zonally-elongated	180	360	30	15	2.96	50.00
4f	T42L30	zonally-elongated	90	180	0	15	2.38	25.00
4g	T42L30	zonally-elongated	90	180	7.5	15	2.57	25.00
4h	T42L30	zonally-elongated	90	180	15	15	2.65	25.00
4i	T42L30	zonally-elongated	90	180	22.5	15	2.62	25.00
4j	T42L30	zonally-elongated	90	180	30	15	2.91	25.00
5a	T42L30	compact regional	90	60	0	30	1.45	6.00
5b	T42L30	compact regional	90	60	5	30	1.48	6.00
5c	T42L30	compact regional	90	60	10	30	1.51	6.00
5d	T42L30	compact regional	90	60	15	30	1.54	6.00
5e	T42L30	compact regional	90	60	20	30	1.57	6.00
6a	T42L30	$0.5Q_{total}$ of 5a–5e	90	60	0	30	0.73	3.00
6b	T42L30	$0.5Q_{total}$ of 5a–5e	90	60	5	30	0.74	3.00
6c	T42L30	$0.5Q_{total}$ of 5a–5e	90	60	10	30	0.75	3.00
6d	T42L30	$0.5Q_{total}$ of 5a–5e	90	60	15	30	0.77	3.00
6e	T42L30	$0.5Q_{total}$ of 5a–5e	90	60	20	30	0.78	3.00
6f	T42L30	$2Q_{total}$ of 5a–5e	90	60	0	30	2.91	12.00
6g	T42L30	$2Q_{total}$ of 5a–5e	90	60	5	30	2.96	12.00
6h	T42L30	$2Q_{total}$ of 5a–5e	90	60	10	30	3.01	12.00
6i	T42L30	$2Q_{total}$ of 5a–5e	90	60	15	30	3.07	12.00
6j	T42L30	$2Q_{total}$ of 5a–5e	90	60	20	30	3.13	12.00
7a	T85L30	compact regional	90	60	0	30	1.48	6.00
7b	T85L30	compact regional	90	60	5	30	1.49	6.00
7c	T85L30	compact regional	90	60	10	30	1.50	6.00
7d	T85L30	compact regional	90	60	15	30	1.54	6.00
7e	T85L30	compact regional	90	60	20	30	1.58	6.00
7f	T42L60	compact regional	90	60	0	30	1.46	6.00
7g	T42L60	compact regional	90	60	5	30	1.48	6.00
7h	T42L60	compact regional	90	60	10	30	1.51	6.00
7i	T42L60	compact regional	90	60	15	30	1.54	6.00
7j	T42L60	compact regional	90	60	20	30	1.57	6.00
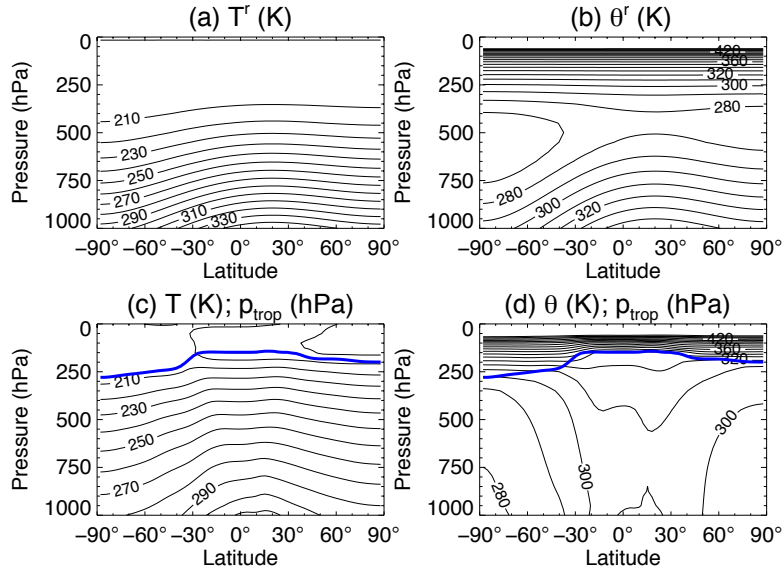
Figure 4.1: (top) Basic state for all numerical experiments: (a) reference temperature T^r and (b) reference potential temperature θ^r. (bottom) Zonal-mean climatology of run 1a with no thermal forcing (control experiment for all simulations at T42L30 resolution): (c) temperature T and (d) potential temperature θ. The tropopause pressure p_{trop} is shown in blue in (c) and (d). Contour intervals of all temperature fields are 10 K. Contours of θ and θ^r above 450K are omitted.

$\times$ longitude on a Gaussian grid), and 30 evenly spaced vertical levels between $\eta \approx 0.9833$ and 0.0167. To test the model sensitivity, several experiments are repeated at T85 horizontal resolution ($\sim 1.4° \times \sim 1.4°$) while other experiments use an L60 vertical resolution (60 evenly spaced vertical levels between $\eta \approx 0.9917$ and 0.0083). The model is initialized with a resting isothermal atmosphere at 250 K. To satisfy the numerical stability criterion, the model time step size is set to 900 (450) s for T42 (T85) experiments. To prevent energy accumulation at small-scales, the biharmonic dissipation coefficient is set to 1.17×10^{16} (7.14×10^{14}) m^4 s^{-1} for T42 (T85) experiments, with a damping time scale of 12 hours at the smallest wavelength (MacVean, 1983).

The zonally symmetric basic state temperature profile T^r is the same in all experiments, as shown in Figures 4.1a and 4.1b (cf. Figure 1 of Held and Suarez (1994) and Figures 1 and 3 of Schneider (2004)). The asymmetry constant $\phi_0^r = 20°$N mimics the boreal atmosphere near the summer solstice. Inspection of time series of various model parameters shows that the transient

response from the isothermal initial condition is negligible after about 300 days. Therefore, the first 300 days of each simulation is discarded as model spin-up. The remaining 300 days, which are sampled four times per day, are used to compute circulation statistics. Figures 4.1c and 4.1d show the resulting climatology from run 1a at T42L30 resolution. Compared to the basic state, the meridional gradient of the zonal-mean surface temperature is reduced because of the poleward and upward energy transport by baroclinic eddies (Schneider, 2004).

Runs 1b and 1c, which are integrated at T85L30 and T42L60 resolution, respectively, produce a very similar climatology (not shown). Increasing horizontal resolution leads to a slightly stronger boreal (weaker austral) subtropical jet, a somewhat stronger winter Hadley cell, and a lower tropical temperature near the surface. Increasing vertical resolution results in slightly stronger subtropical jets in both hemispheres, a relatively stronger winter Hadley cell, and a rather lower temperature at the cold point tropical tropopause.

5. VORTEX BEHAVIOR OF THE ASIAN MONSOON ANTICYCLONE

5.1 Eulerian Vortex Properties

Using the multiple-center method described in Chapter 3.1, the longitudes, latitudes, and Montgomery streamfunction Ψ of sub-vortices within the AMA are computed for each 6-hourly ERA-Interim reanalysis for 00 UTC on May 1 through 18 UTC on September 30 for the 39-year period from 1979 to 2017. This comprises a total of 23,868 analysis times. The analysis domain extends from 180°W to 180°E and 0° to 60°N, but the Eulerian vortex statistics are computed only for the region from 0° to 180°E and 15° to 45°N. The total number of individual vortices for the entire analysis period is 64455 (Table 5.1).

Table 5.1: Count and frequency of the number of vortices in each month of warm season for the entire analysis period (1979–2017).

	All	Transient vortices		Persistent vortices	
Month	count	count	percentage	count	percentage
May	12296	4468	36.3	7828	63.7
June	11300	2590	22.9	8710	77.1
July	12546	1867	14.9	10679	85.1
August	14019	2212	15.8	11807	84.2
September	14264	3361	23.6	10903	76.4
Total	64455	14498	22.5	49957	77.5

5.1.1 Vortex Evolution

The evolution of monsoon sub-vortices for 2017 is shown in Figure 5.1. Dots represent each identified vortex centers; persistent and transient sub-vortices are colored in red and blue, respectively, according to the definitions in Chapter 3.1. Persistent sub-vortices are connected by black lines. Compared to the total number of all individual vortices, the persistent vortices account for
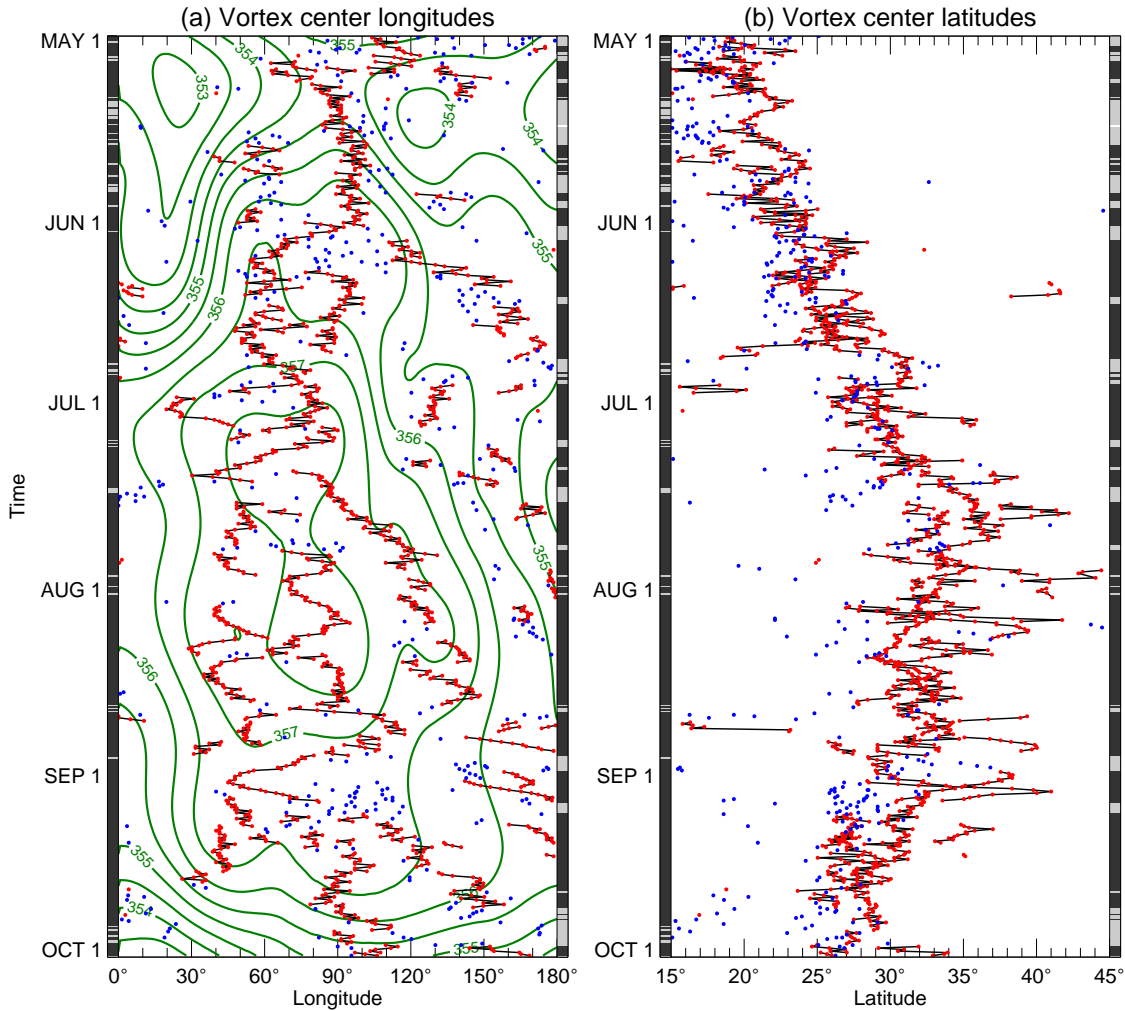
Figure 5.1: (a) Longitude-time plot of all identified vortex centers (dots) in the region of 0°–180°E and 15°–45°N for May through September of 2017. Persistent and transient vortices are colored in red and blue, respectively. Persistent vortices are also connected by black lines. The total number of persistent and transient vortices in 2017 are 1387 and 413, respectively. Hovmöller plot of ERA-Interim Montgomery streamfunction Ψ of 2017 (green contours; interval: 0.5 kJ kg^{-1}). The time series of Ψ is averaged and smoothed the same way as in Figure 1.2. (b) as in (a) but a latitude-time plot. (a)–(b) The colored bars along the left edge indicates the number of vortices present at each analysis time, while the colored bars along the right edges indicate the number of persistent vortices present at each analysis time (white $=$ 0, light gray $=$ 1, dark gray $\geq$ 2).

77.1% and 77.5% of the population for 2017 and the whole analysis period, respectively (Table 5.1).

Figure 5.1a is overlaid with the Montgomery streamfunction Ψ (green contours), which is

smoothed as in Figure 1.2. The lifecycle of the AMA is similar to the climatology. For example, weak vortices occur during the onset of the AMA in May or away from the main vortex throughout the warm season. The spin-up of the AMA during May and June and its dissipation during late September occur more rapidly than in the climatology, which is smoothed by interannual variations. During the mature stage in July and August, vortices are found near 60° and 90°E, where Ψ is largest. But multiple persistent vortices are found at other longitudes as well. Over the course of the warm season, the locations of vortices and the latitude of the overall AMA center shift first poleward and then equatorward (Figure 5.1b).

The colored bars along the left and right edges of the plot indicate the number of individual vortices and the number of persistent vortices, respectively, that are present at each analysis time (white for zero, light gray for one, and dark gray for two or more vortices). Two occasions of zero persistent vortices happen in May only. One persistent vortex usually happen in the beginning and end of the warm season. Transient vortices are seen intermittently at various times in different parts of the domain. Some groups of vortices that appear to be closely clustered in space and time are not identified as persistent. Examples can be seen near 60°E in the second half of May. These clusters are not tagged as persistent vortices because they do not meet the criterion for four sequential analysis times.

As will be shown in Chapter 5.2, persistent vortices are more interesting in characterizing several types of observed vortex behavior. Table 5.2 shows the frequency distribution of the number of persistent vortices present at each analysis time for 2017 and for the entire analysis period. Most of the time there are two or more vortices (73.5%). Cases of zero (0.3%) and one (26.1%) vortex are infrequent and occur most often in May and September. Because vortices of similar strength often occur at the same analysis time, as shown in Figure 5.1a, selecting only the strongest vortex misses much of the structure of the overall AMA circulation. Overall there is one vortex 23.4% of the time, but more often two and three vortices are present (69.4% combined). Rarely are there either zero (1.9%) or four or more (5.3%) vortices.

Figure 5.2 shows that the climatological number of all sub-vortices in general increases over

30

Table 5.2: Count and frequency of the number of persistent vortices present at each analysis time.

Number	2017		1979–2017	
	count	percentage	count	percentage
0	2	0.3	455	1.9
1	160	26.1	5581	23.4
2	201	32.8	10524	44.1
3	183	29.9	6034	25.3
≥ 4	66	10.8	1274	5.3
Total	612		23868	
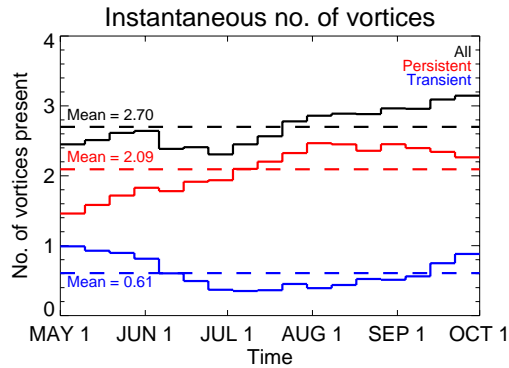
Figure 5.2: Climatological averages of the instantaneous number of vortices for the analysis period 1979–2017 (black: all; red: persistent only; blue: transient only). To reduce the noise, instantaneous values are averaged into 9-day intervals. The overall time average for all vortices is 2.70.

the course of the warm season. The average number of all vortices present is 2.70. But persistent and transient vortices show opposite trends. While there are more transient vortices towards the beginning and the end of the warm season, the number of persistent vortices peaks in August.

There are significant variations in the vortex behavior from year to year. The average instantaneous number of all sub-vortices ranges from 2.27 in 1995 to 3.14 in 2015. In some years, such as 1994, the longitudes of vortices are relatively stationary. In other years, such as 2010, long-lived vortices drift slowly westward; when they reach longitudes near $45°$E, new vortices form near $90°$E.
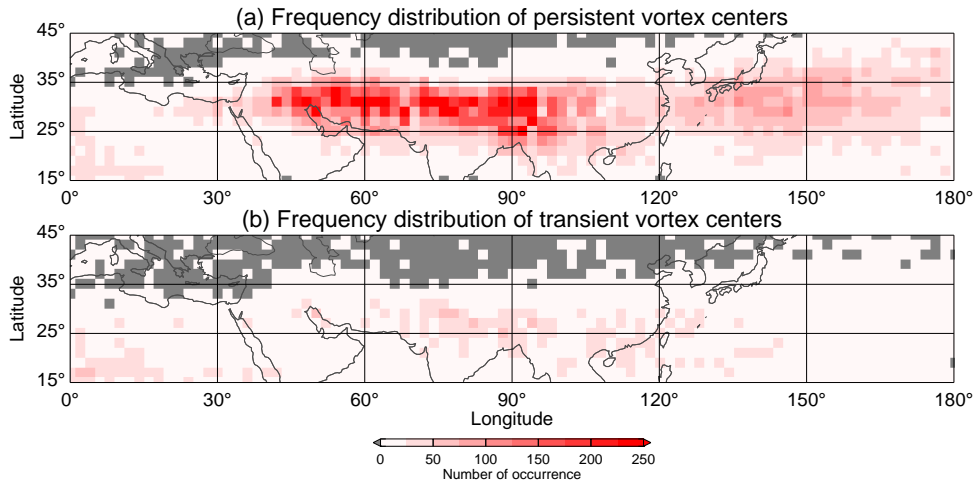
Figure 5.3: Two-dimensional frequency distributions for the analysis period (1979–2017). (a) Persistent vortices. (b) Transient vortices. Bin size is $2° \times 2°$. Bins with zero occurrence of vortex centers throughout the analysis period colored gray. The total number of persistent and transient vortices are 49957 and 14498, respectively. Corresponding one-dimensional frequency distributions for longitude and latitude of persistent vortices are plotted in Figures 5.4a and 5.4b, respectively.

Most years have several vortex splitting and merger events, an example of which will be discussed below.

5.1.2 Geographical Distribution of Sub-vortices

Most of the time there are two or more vortices in the domain simultaneously, so it is of interest to see the geographical distributions of the vortex centers. Figure 5.3 shows the frequency distribution of persistent and transient vortices for the entire period grouped $2° \times 2°$ bins. Note that the area of a bin centered at 45°N is only $\sim 73\%$ of a bin centered at 15°N.

For the persistent vortices, Figure 5.3a is similar to Figure 1 in Nützel et al. (2016) which uses the ERA-Interim daily geopotential height field at 100 hPa for 1979–2014 from June to August. While high occurrence frequencies are concentrated in the region of 45°–100°E and 25°–35°N as in Nützel et al. (2016), we also notice that there is an expansive area of higher frequency between 120° and 180°E. Because these vortices tend to be weaker than vortices over the Asian continent, they are often not detected by the single-vortex method used in Nützel et al. (2016). This area also

extends to a wider range of latitudes compared to vortices over the continent. Figure 5.3b shows that the transient vortices occur more frequently at lower latitudes than the persistent vortices and are uncommon east of 150°E.

Figure 5.4a displays histograms of the longitudes of vortex centers for the entire period. There are two broad peaks. The first one, between about 40°E and 100°E, is associated with what have previously been labeled the Iranian and Tibetan Highs. In the aggregate plot (black curve), these two modes are not clearly separated. The second maximum, which peaks near 150°E and represents the Bonin High, has received much less attention in the literature because it is usually regarded as a subtropical anticyclone which is not present in the upper troposphere in the early summer but exhibits a deep vertical structure extending through the whole troposphere in late July and August (Enomoto et al., 2003). Its formation mechanism has been deemed to be different from the Tibetan and Iranian Highs (Enomoto et al., 2003).

Because we identify multiple simultaneous vortices, additional analysis is possible. The histograms in Figure 5.4 are stratified by the instantaneous number of persistent vortices present. When a single vortex is present (red), the AMA is most likely to be centered between 60°E and 100°E and is rarely found west of 40°E and east of 120°E. Only when two or more vortices are present does the Bonin High peak emerge. Therefore, any method that assumes the existence of a single center is unlikely to detect the Bonin High. For example, although the eastern end of the domain in Nützel et al. (2016) is 140°E, the occurrence of centers distinctly drops east of 120°E. We interpret the results differently from Zhang et al. (2002) and Nützel et al. (2016). Rather than seesawing between the Iranian mode near 90°E and the Tibetan mode near 60°E, the main variation is between states with multiple (mainly two or three) persistent vortices within the main AMA circulation.

The peaks representing the Tibetan and Iranian Highs are easier to distinguish in some months. In May, most of the time there are either one or two vortices. The Tibetan High starts off as the dominant peak (Figure 5.4c), especially when only one peak is present (red). As the AMA strengthens in June, both the Tibetan and Iranian Highs stand out when there are two to three vortices (Figure

33
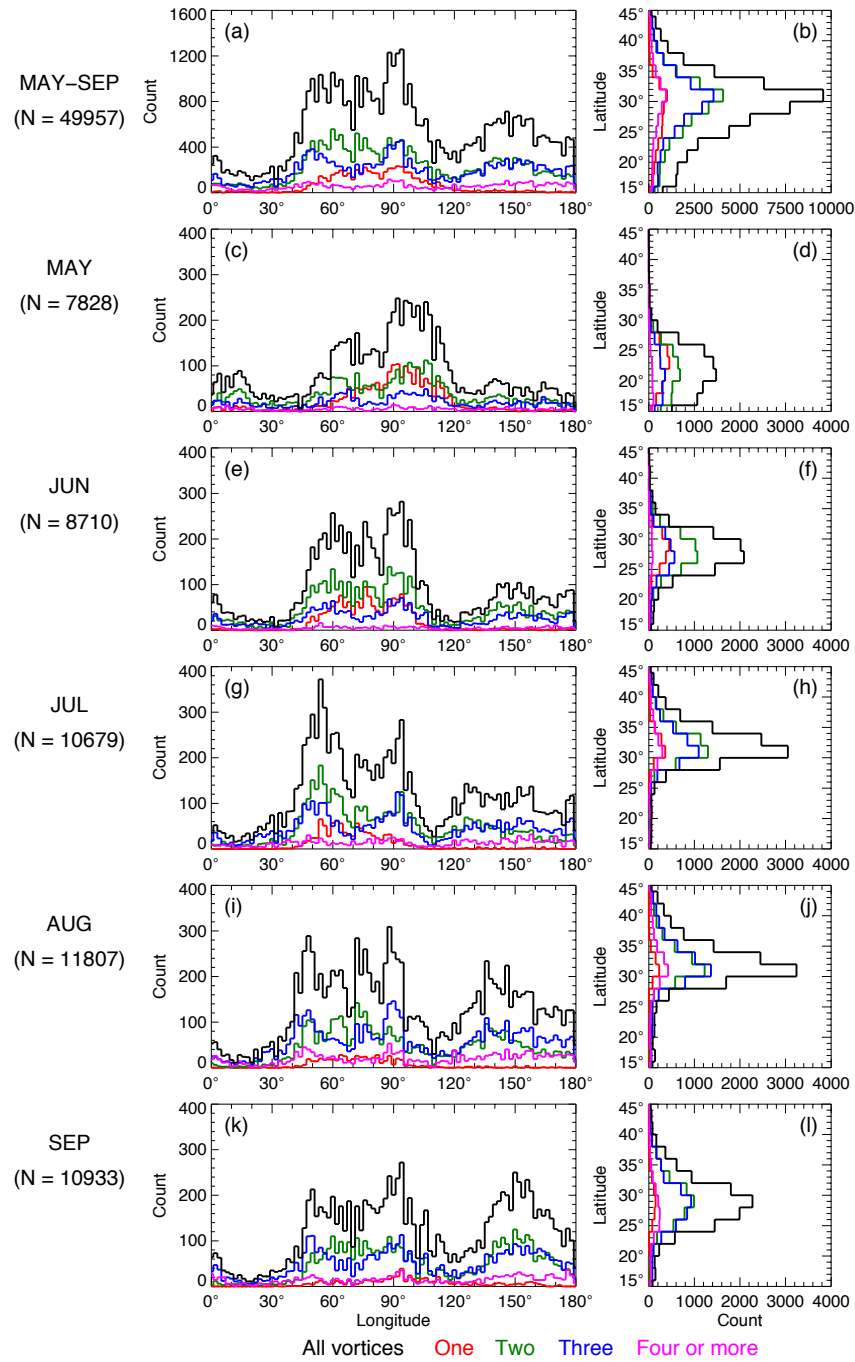
Figure 5.4: Overall and conditional histograms of the longitude (left) and latitude (right) of persistent vortices for the analysis period (1979–2017). Each bin is 2°. (a),(b) All months. (c),(d) May. (e),(f) June. (g),(h) July. (i),(j) August. (k),(l) September. Total number of persistent vortices is labeled for each period. Black: histogram for all persistent vortices. Red: histograms when one vortex is present. Green: histograms when two vortices are present. Blue: histograms when three vortices are present. Magenta: histograms when four or more vortices are present.

34

5.4e). In contrast to Enomoto et al. (2003), we find that the Bonin High manifests in June, usually appearing when there are also one or two vortices over the continent. In July, the Iranian and Tibetan Highs are still the dominant peaks (Figure 5.4g). When there are three vortices, there are three distinct modes in the distribution. Also, the primary peak shifts to the Iranian High ($\sim 60°$E) when there are two vortices. In August and September, single-vortex state becomes rare and no distinct peak is seen (Figures 5.4i and 5.4k). The peaks of the Tibetan and Iranian Highs are difficult to be distinguished but the Bonin High peak becomes much sharper. The total number of persistent vortices increases from May, peaks in August, and slightly drops in September (Table 5.1). These results reveal details of the time series in Figure 5.2b. The increasing number of vortices throughout the season is mainly due to the appearance of the Bonin High.

The panels in the right-hand column of Figure 5.4b show the latitudinal distributions of the vortex centers. In the zonal direction a single peak is found near 30°N. All months exhibit a single peak independent of the number of vortices present. The latitude of the peak is also independent of the number of vortices present but does depend on month. As the AMA spins up in May, vortices are primarily located equatorward of 25°N (Figure 5.4d). Once the AMA is at the mature stage, there is a single peak near 30°N (Figures 5.4h and 5.4j). In the interim as the AMA strengthens in June and weakens in September, the peak broadens (Figures 5.4f and 5.4l).

5.2 Vortex Behavior

In this section we present case studies of vortex behavior that are commonly observed within the AMA. These include vortex splitting and merger, and eastward and westward eddy shedding. Note that in the current method there is no objective way to differentiate between vortex splitting and eddy shedding. In other contexts, such as flow past an obstacle, 'eddy shedding' is conventionally used to refer to the (quasi-)periodic vortex coherent vortices (Kundu et al., 2016). Given the size of the AMA circulation (Figure 1.1), however, it is difficult to determine whether an eddy and the parent vortex are separated. In practice, we define a westward (eastward)-shedding event as an eddy is separated from the AMA circulation and crosses 0° (180°E).

35

5.2.1   Vortex Splitting and Merger

Sub-vortices within the AMA usually undergo several split-merger cycles during the warm season (see, for example, June, July, and August in Figure 5.1). The details of the flow evolution vary each year, but there are two identifiable types of vortex split-merger events. The first occurs between 30° and 120°E and does not involve the Bonin High. The evolution of one such event during June and July of 2009 is highlighted with a gray background in Figure 5.5a. Analyses of Montgomery streamfunction Ψ and zonal wind u for selected times are given in Figures 5.5b–g. The time of each analysis is indicated by dashed lines in Figure 5.5a. Plotting conventions are the same as Figure 3.2a.

Between June 25 and 29, a single persistent vortex is present near 90°E (Figures 5.5a and 5.5b). The main vortex expands eastward and then splits into two sub-vortices around 1 July (Figure 5.5c). The two sub-vortices continue to separate, reaching their maximum separation around 4 July (Figure 5.5d). Thereafter, the distance of separation decreases (Figures 5.5e and 5.5f) and the vortices merge around 10 July (Figure 5.5g). The entire process takes about 2 weeks. Another vortex splitting event occurs shortly after 11 July (Figure 5.5a).

Fluid motions during this vortex split-merger event are illustrated in Figure 5.6 through the use of trajectories. The M field is displayed in grayscale in the background. Contours of Ψ are overlaid in blue. Two patches of fluid marking the two sub-vortices ($\Psi \geq 356.85$ kJ kg^{-1}) are selected from the time of maximum separation of the sub-vortices, 12 UTC on 4 July 2009 (Figure 5.6c). Fluid in the western and eastern vortices is colored green and red, respectively. Backward and forward trajectories are used to determine where the fluid in the sub-vortices came from, and how it was stirred together when the vortices merged. The M values of the sub-vortex interiors are comparatively low (dark gray), indicating the fluid does not move large distances.

At the beginning of the splitting event, the fluid that will form the western sub-vortex is located on the north side of the AMA, while the fluid that forms the eastern sub-vortex is located to the south (Figure 5.6a). These patches rotate around each other in the primary AMA flow. The two patches of fluid separate around 1 July as the single vortex splits into two distinct sub-vortices

36
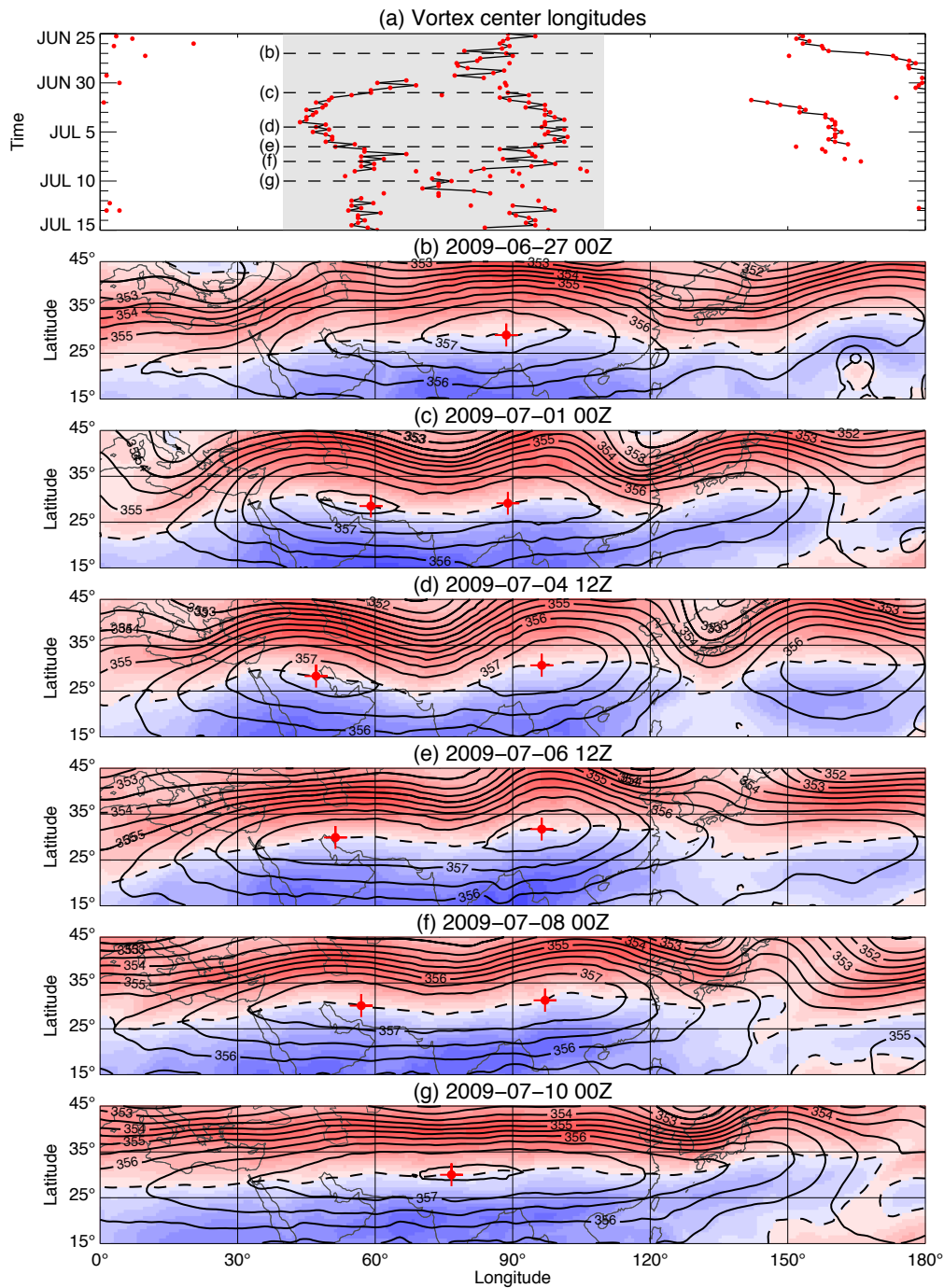
Figure 5.5: An example of the first type of vortex split-merger event. (a) Evolution of this event during late June and early July 2009, which is highlighted with a gray background. Vortex centers are colored in red and persistent vortices are connected with black lines. Snapshots (b)–(g) Snapshots of this event are labeled and indicated by dashed lines in (a). Zonal wind u (red: $u > 0$; blue: $u < 0$, dashed line: $u = 0$; interval: 5 m s^{-1}) and Montgomery streamfunction Ψ (black contours; interval: 0.5 kJ kg^{-1}) on the 370 K isentropic surface. Vortex centers are indicated by red crosshairs. For clarity, only those vortex centers that are highlighted in (a) are shown.
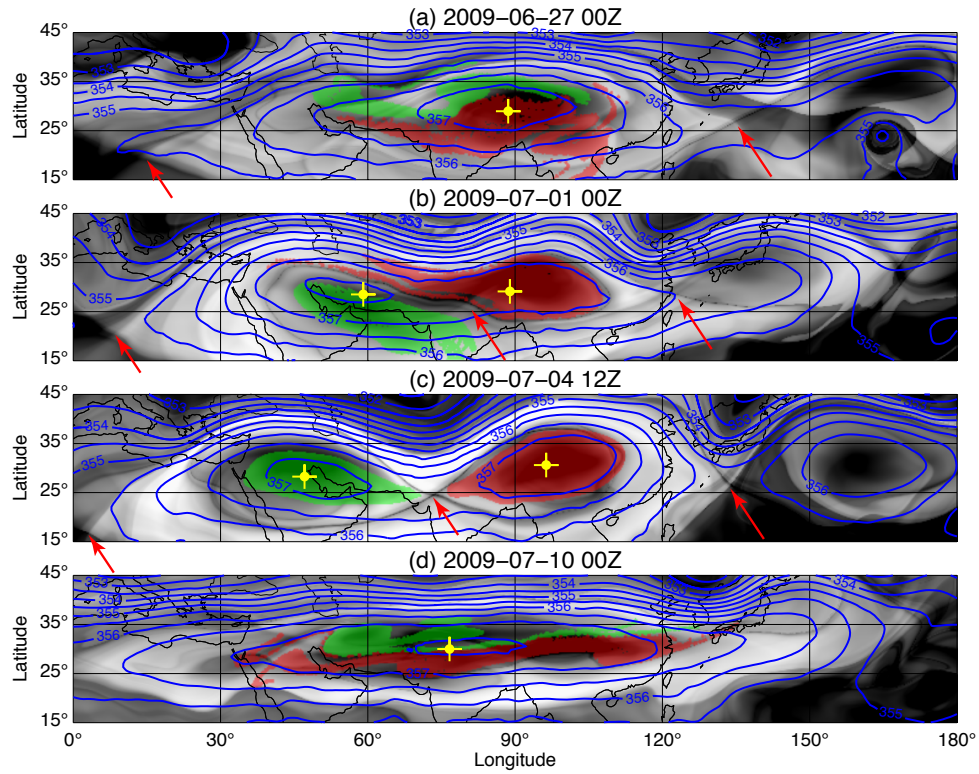
Figure 5.6: Snapshots of trajectories during the first type of vortex split-merger event shown in Figure 5.5. Montgomery streamfunction Ψ (blue contours; interval: 0.5 kJ kg^{-1}) and M (grayscale) are plotted on the 370 K isentropic surface. Particle positions (red and green) are from forward and backward trajectories initialized at the time of (c). Particles are colored the same in all panels based on which of the two vortices they are located in (c). Vortex centers are indicated by yellow crosshairs. For clarity, only those vortex centers that are highlighted in Figure 5.5a are shown. Some hyperbolic regions are indicated by red arrows.

(Figure 5.6b) and the new hyperbolic region emerges between them (middle arrow; c.f. Figure 1 of de la Cámara et al. (2013)). Each patch moves into the core of its respective vortex Figures 5.6b and 5.6c). Subsequently, the hyperbolic region in the interior of the AMA disappears as the two sub-vortices weaken. In the absence of a hyperbolic region, the fluid from the two sub-vortices is stirred slowly by the single primary AMA vortex (Figure 5.6d). During the merger (4–10 July), the fluid within each sub-vortex makes one complete revolution around the main AMA circulation.

The second type of vortex split-merger events is associated with the Bonin High. An example of the evolution of this type during late August and early September of 2004 is highlighted with gray background in Figure 5.7a. Several snapshots with contours of Ψ are shown in Figures 5.7b–g. In late August, the AMA circulation is in the mature stage, extending over $180°$ in longitude (Figure 5.7b). East of $120°$E, two sub-vortices consecutively break off from the Tibetan and Iranian Highs, which are indicated by black arrows in Figure 5.7a. When the separation of these two sub-vortices happens, the low PV area is also consistently extended eastward (not shown). West of $120°$E, two persistent vortex centers that can be identified as Tibetan and Iranian Highs persist until they merge around 6 September (Figures 5.7b–f). That merger belongs to the first type of vortex split-merger events. Therefore two kinds of vortex split-merger events can take place simultaneously.

Fluid motions for these two types of vortex split-merger events are shown through the use of trajectories in Figures 5.7b–g. Two patches of fluid within the AMA are selected from the analysis time 12 UTC on 2 September 2004 (Figure 5.7d). The first one ($\Psi \geq 356.75 \text{ kJ kg}^{-1}$), representing the core part of the Tibetan and Iranian Highs, is colored red; the second one ($\Psi \geq 356.5 \text{ kJ kg}^{-1}$), representing the core part of the Bonin High, is colored green.

Backward trajectories show that the green and red particles are intermingled within the main AMA circulation on 26 August (Figure 5.7b). Note the hyperbolic region between the two persistent sub-vortices (middle arrow). The green particles move along the northern side of the AMA circulation (Figures 5.7b and 5.7c). By 2 September the green and red particles lie within distinct sub-vortices separated by the emergence of another hyperbolic region near $130°$E (Figure 5.7d). The sub-vortex of the Bonin High persists for around a week. As the Bonin High dissipates (Figure
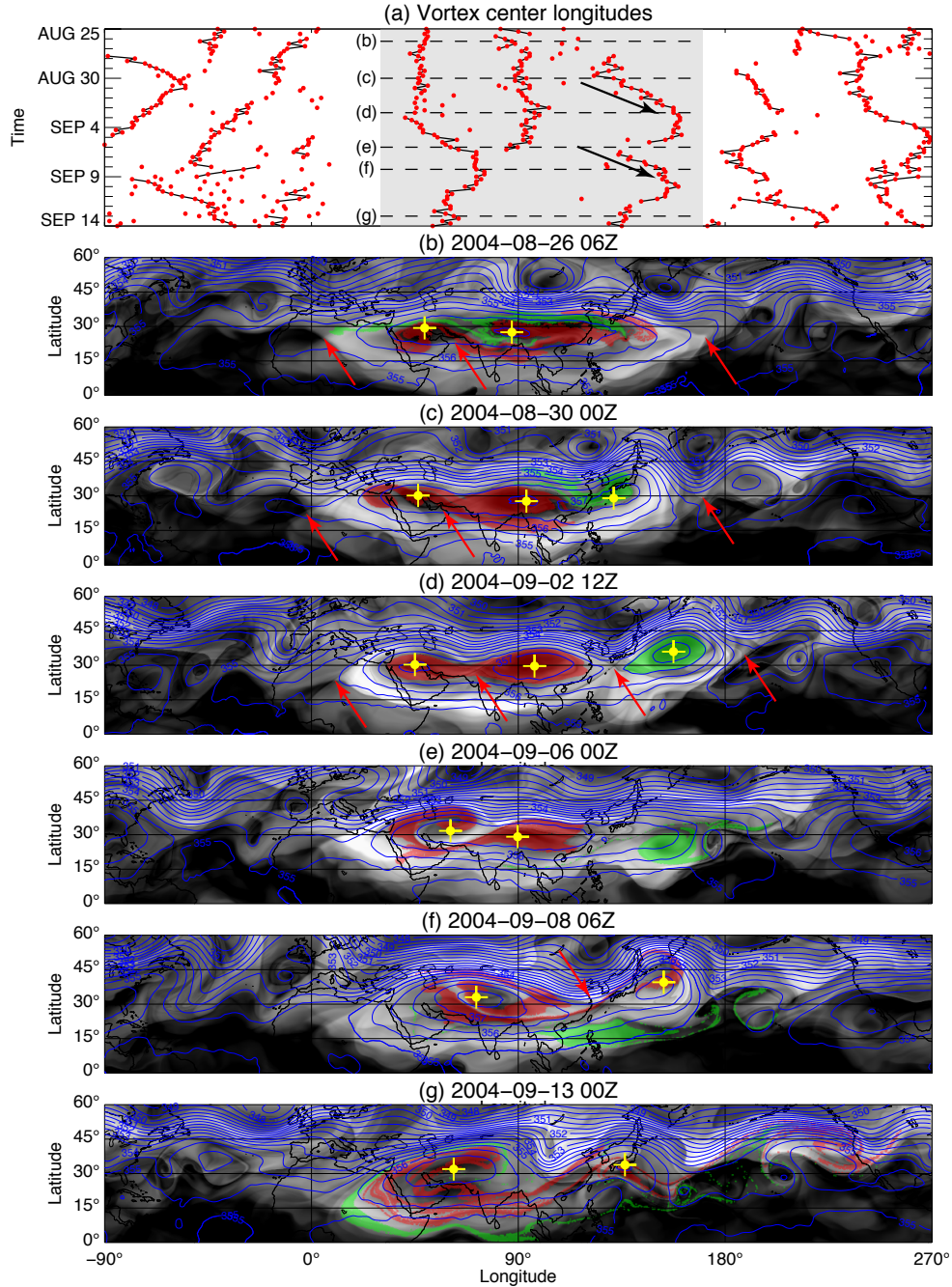
Figure 5.7: An example of the second type of vortex split-merger event. (a) Evolution during late August and early September 2004, highlighted with a gray background. Vortex centers are colored in red and persistent vortices are connected with black lines. Movements of two splitting events east of 120°E are indicated by black arrows. (b)–(g) Snapshots of this event are labeled and indicated by dashed lines in (a). Montgomery streamfunction Ψ (blue contours; interval: $0.5\,\mathrm{kJ\,kg^{-1}}$) and M (grayscale) are plotted on the 370 K isentropic surface. Particle positions (red and green) are from forward and backward trajectories initialized at the time of (d). Particles are colored the same in (b)–(g) based on which of the vortices they are located in (d). Vortex centers are indicated by yellow crosshairs. For clarity, only those vortex centers that are highlighted in (a) are shown. Some hyperbolic regions are indicated by red arrows.

40

5.7e), the fluid within is advected westward around the southern side of the primary AMA, where it is stretched and entrained back into the main AMA (Figures 5.7f and 5.7g). It is then wrapped all the way around the western side and into the interior. While this is happening, the separate Tibetan and Iranian Highs merge.

5.2.2 Eastward Eddy Shedding

Figure 5.1a shows that for 2017 most of the identified vortices near 180°E are usually weak and transient (blue). Exceptions are seen for some persistent vortices (red) in late August and early September. In this time period two eastward eddy-shedding events can be clearly identified, one of which is shown in detail in Figure 5.8a. The black arrow highlights the motion of the vortex in question. Several snapshots with contours of Montgomery streamfunction Ψ are shown in Figures 5.8b–g. A patch of fluid within the AMA ($\Psi \geq 356.5$ kJ kg^{-1}) is selected from the analysis time 00 UTC on 23 August 2017 (Figure 5.8c). There are two sub-vortices within this patch of fluid, one being relatively stronger and covering a larger area near 100°E. Note the hyperbolic region between these two vortices (arrow). To examine the validity of the 'pinch-off' process illustrated in Figure 1.3, the particles inside the core region of the stronger vortex ($\Psi \geq 357$ kJ kg^{-1}) are tagged in red, while the outer region is tagged in green.

Backward trajectories show that the red particles come from two sub-vortices of similar strength in the previous split-merger event as shown in Figure 5.8b. The red patch of air is brought together by the converging flow near the hyperbolic region ('reverse filamentation') seen in Figures 5.8b and 5.8c. Forward trajectories show that the stronger vortex (red) becomes elongated around 25 August (Figure 5.8d). A hyperbolic region emerges (right arrow) and then a new sub-vortex center forms east of the original vortex near 135°E shortly after 25 August. Most of the air is from the core of the original eastern vortex (red), with filaments (green) from the outer region (Figures 5.8e and 5.8f). This fluid organizes to form a Bonin High (Figure 5.8e).

The early flow evolution is similar to the second identifiable type of vortex split-merger events (Figure 5.7). But unlike the previous split-merger case, this sub-vortex does not dissipate and

41
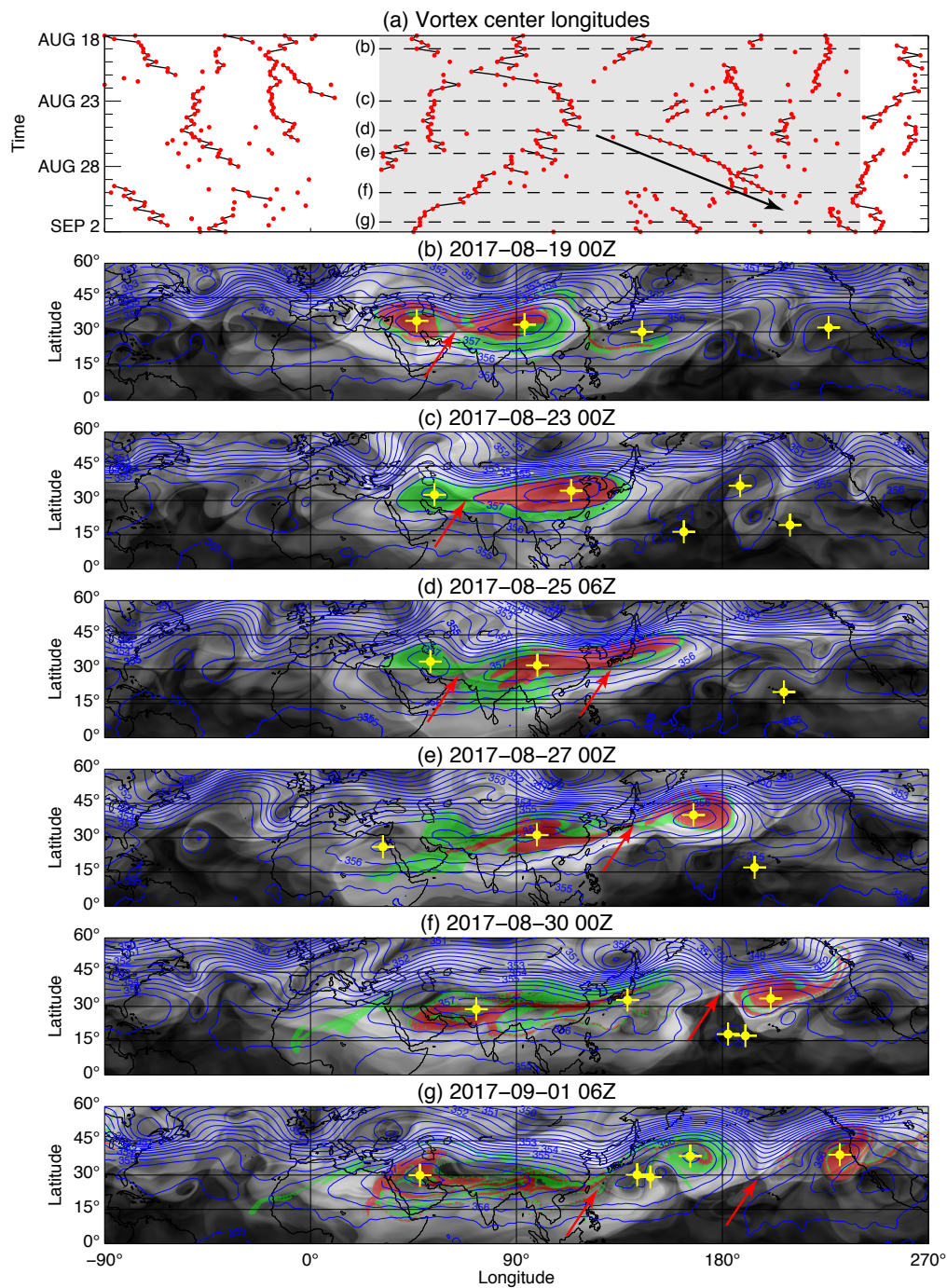
Figure 5.8: Same as Figure 5.7 for an eastward eddy-shedding event during August and early September 2017. Particle positions (red and green) are from forward and backward trajectories initialized at the time of (c). (a) Evolution is highlighted with a gray background. Movements of the eastward shedding eddy are indicated by the black arrow. (b)–(g) For clarity, only those vortex centers that are highlighted in (a) are shown.

recirculate into the main AMA circulation. The eddy maintains its identity, propagates eastward along the southern flank of the subtropical jet, and enters the Western Hemisphere around 28 August (Figures 5.8e and 5.8f). The circulation is maintained for several more days before merging with the NAMA. The red particles are entrained into the core of the NAMA circulation and arrive at the west coast of the United States near 1 September (Figure 5.8g). The entire shedding process takes about ten days. A second eastward eddy-shedding event is happening east of the dateline at the same time (Figure 5.8g). Note that most of the green particles that form this second eddy were located on the western side of the AMA a few days earlier (Figure 5.8d). This illustrates the complex history of the air contained within eddies 'pinched off' from the main AMA circulation.

5.2.3 Westward Eddy Shedding

As can be seen in Figure 5.4, vortices occur infrequently west of 30°E, which implies that westward eddy-shedding events are not common. Nevertheless, some westward-moving eddies are observed in the seasonal vortex plots. One particularly coherent and long-lived event, shown in Figure 5.9, occurred during 1999. The steady westward propagation is indicated by the black arrow in Figure 5.9a. Snapshots of corresponding fluid motion are provided in Figures 5.9b–g. Two patches of fluid ($\Psi \geq 356.3$ kJ kg^{-1}) within the sub-vortices are selected from the analysis time 00 UTC on 15 July 1999 as shown in Figure 5.9e.

This eddy-shedding event is preceded by a complete vortex split-merger cycle in early July. A single persistent vortex splits into two sub-vortices which merge back into a single vortex between 4 and 8 July (Figures 5.9a–c). After that, the vortex splits again and forms two sub-vortices around 12 July (Figure 5.9d). The western vortex persists and slowly moves across the prime meridian around 18 July (Figures 5.9e and 5.9f).

Backward trajectories show that the fluid that forms the two vortices in Figure 5.9e was previously intermingled (Figure 5.9b). The red patch forming the core part of the western vortex in Figure 5.9c rotates and moves eastward around the north side of the AMA as the two sub-vortices in Figure 5.9b start to merge. Thereafter a hyperbolic region (red arrow) emerges near 60°E (Figure
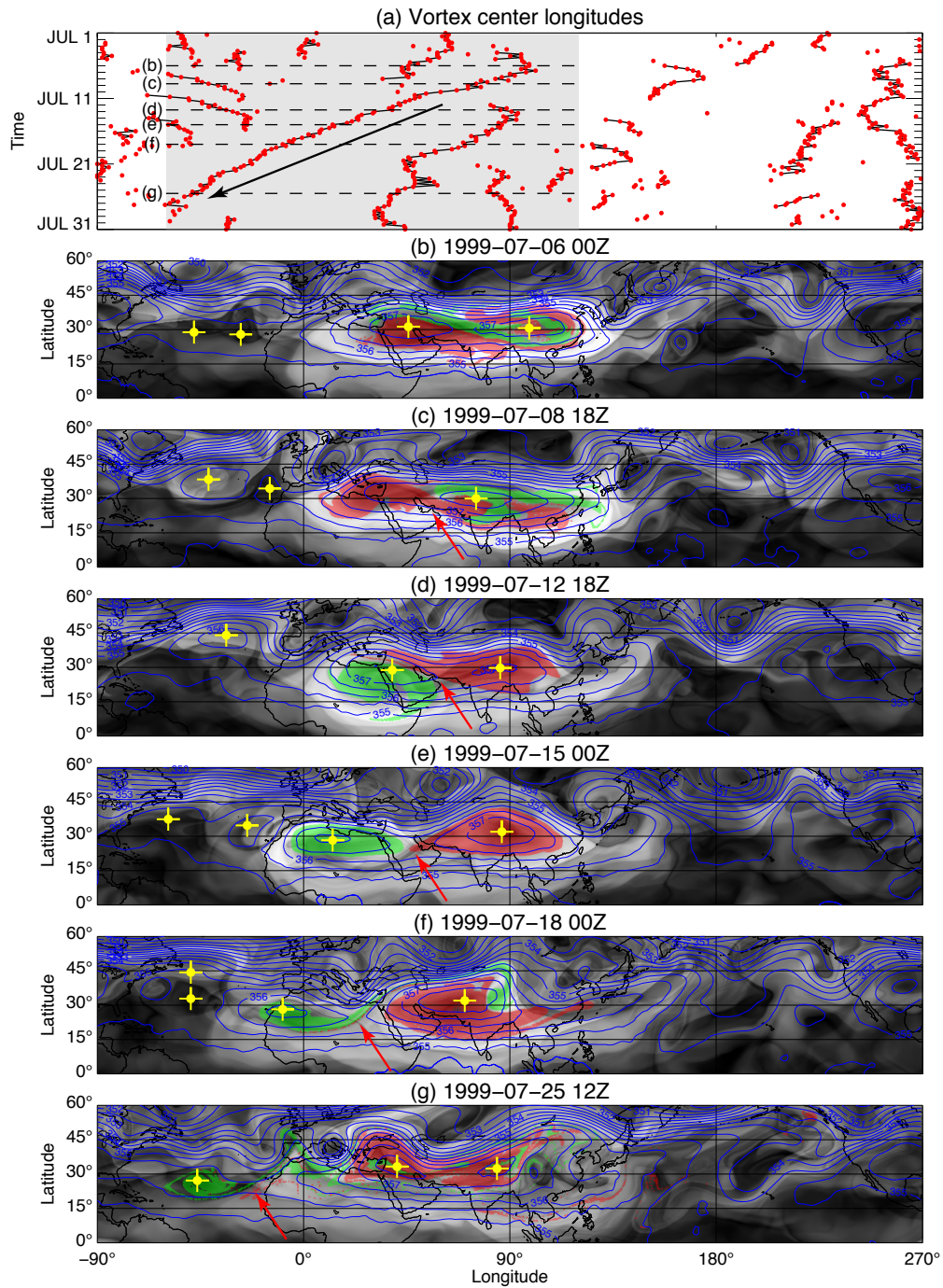
Figure 5.9: Same as Figure 5.7 for a westward eddy-shedding event during July 1999. Particle positions (red and green) are from forward and backward trajectories initialized at the time of (e). (a) Evolution is highlighted with a gray background. Movements of the westward shedding eddy are indicated by the black arrow. (b)–(g) For clarity, only those vortex centers that are highlighted in (a) are shown.

5.9d). The red particles organize and form a new vortex over Tibet around 12 July and similarly green particles form another vortex near 30°E (Figure 5.9d). Over the next two weeks the new western vortex (green) drifts westward as far as 45°W. Some of the air originally in the western vortex is pulled through the hyperbolic region between the two vortices, filamented, and entrained into the eastern vortex (Figures 5.9f and 5.9g). At this point the westward motion of shed vortex stops, and the eddy weakens and dissipates few days later (Figure 5.9a).

5.2.4 Summary

Statistically the plot in Figure 5.1 is typical of the vortex behavior for each year. The tracks of the persistent sub-vortices show that they usually undergo several split-merger cycles throughout the warm season. The patterns vary from year to year, but overall there are two major kinds of vortex split-merger events. The earlier stage of an eddy-shedding event resembles a vortex split which makes the identification process less straightforward. The Eulerian and Lagrangian approaches complement each other to characterize different types of vortex behavior.

6. ORIGIN OF THE NORTH AMERICAN MONSOON ANTICYCLONE[1]

6.1 Response to the Realistic Forcing

6.1.1 Model Tuning

To determine the major forcing regions of the NAMA, numerical experiments are carried out using realistic global and regional geographical distributions of latent heating derived from the TMPA precipitation data. A top-down approach is used to analyze the impacts of various regions on the upper-tropospheric circulation. The model is first subjectively tuned to produce a realistic zonal-mean state and reasonable representations of the AMA and NAMA when forced by latent heating throughout the tropics and subtropics (run 2a). The time-averaged model response to latent heating within selected regions is then examined.

Because of several significant simplifications in the model, including the absence of topography, land–sea contrast, and temporal variations of the heating, a perfect simulation is not expected. To produce the best possible simulation of the monsoon anticyclones, the principal tuning parameter for the basic state is the pole-to-equator temperature gradient Δ_h, while the horizontal distribution Q_h, vertical distribution Q_v, and the strength Q_0 of the thermal forcing also play important roles.

Preliminary experiments show that the subtropical jet strengthens when either the pole-to-equator temperature gradient or the total external thermal forcing increases. To include a representative geographical extent of the forcing region, but at the same time not make the jet too strong, we set $\Delta_h = 30$ K and limit the TMPA-derived forcing to the zone from 5°S to 40°N.

Preliminary experiments also show that the response of the anticyclones is not very sensitive to the vertical extent of the forcing, especially the bottom level p_b, but the shape parameter of the vertical distribution B does matter. The top and bottom levels of the forcing in the vertical direction are set to 100 and 1000 hPa, respectively, and a slightly top heavy profile ($B = 1$) is used in (4.7). Although Barlow et al. (1998) computed the vertical heating profile over Mexico from
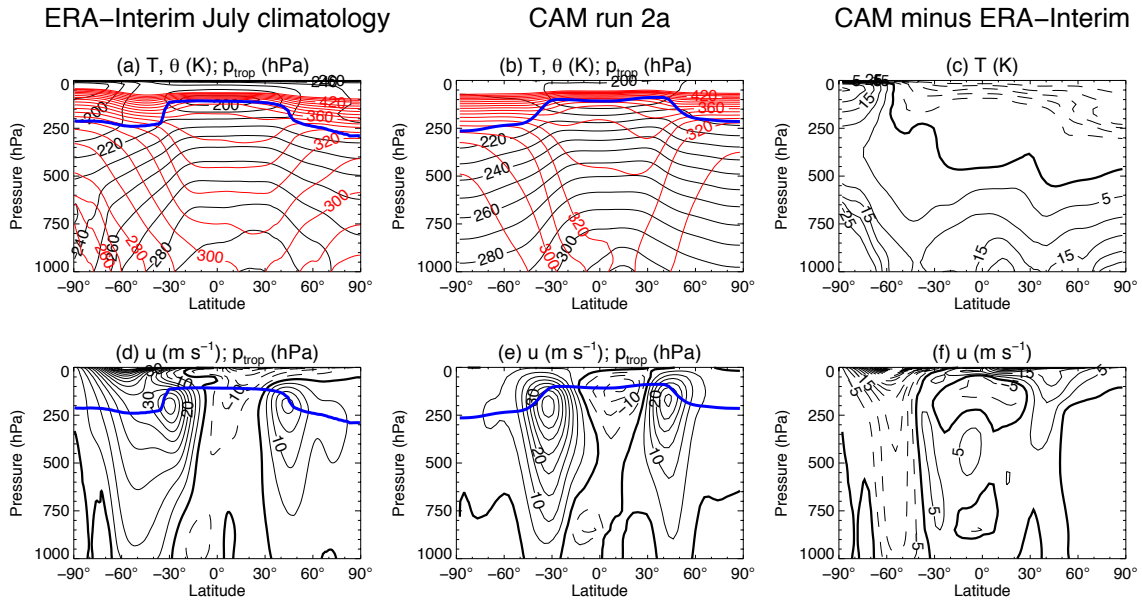
Figure 6.1: Latitude–pressure cross sections of selected time-mean, zonal-mean fields. (left) ERA-Interim July climatology. (center) CAM run 2a. (right) Difference (CAM minus ERA-Interim). (a),(b) Temperature T (black) and potential temperature θ (red). (c) Temperature T. (d)–(f) Zonal wind u. The tropopause pressure p_{trop} (blue) is shown in the left and middle columns. Contour intervals of T for (a) and (b) are 10 K and (c) are 5 K. Contour intervals of θ and u are 10 K and 5 m s^{-1}, respectively. Negative values are dashed, and zero values of T and u are in bold contours. Contours of θ above 450 K are omitted.

two reanalyses and found that there are double maxima at 200 hPa and 400 hPa, the current profile used over the whole domain has a single peak near 450 hPa.

Finally, the forcing magnitude parameter Q_0 of run 2a is adjusted to produce the best response. Within the forcing region, the total observed latent heat of condensation computed from (4.8) is approximately 187.95×10^{19} J day^{-1} (Table 4.2). The most realistic response is found for $Q_0 = 6.35$ K day^{-1}, which corresponds to approximately 59% of the observed amount of latent heating computed from (4.9). Attempting to adjust the model by increasing Q_0 closer to 100% of the observed heating and decreasing Δ_h to compensate, changes the general circulation in undesirable ways.
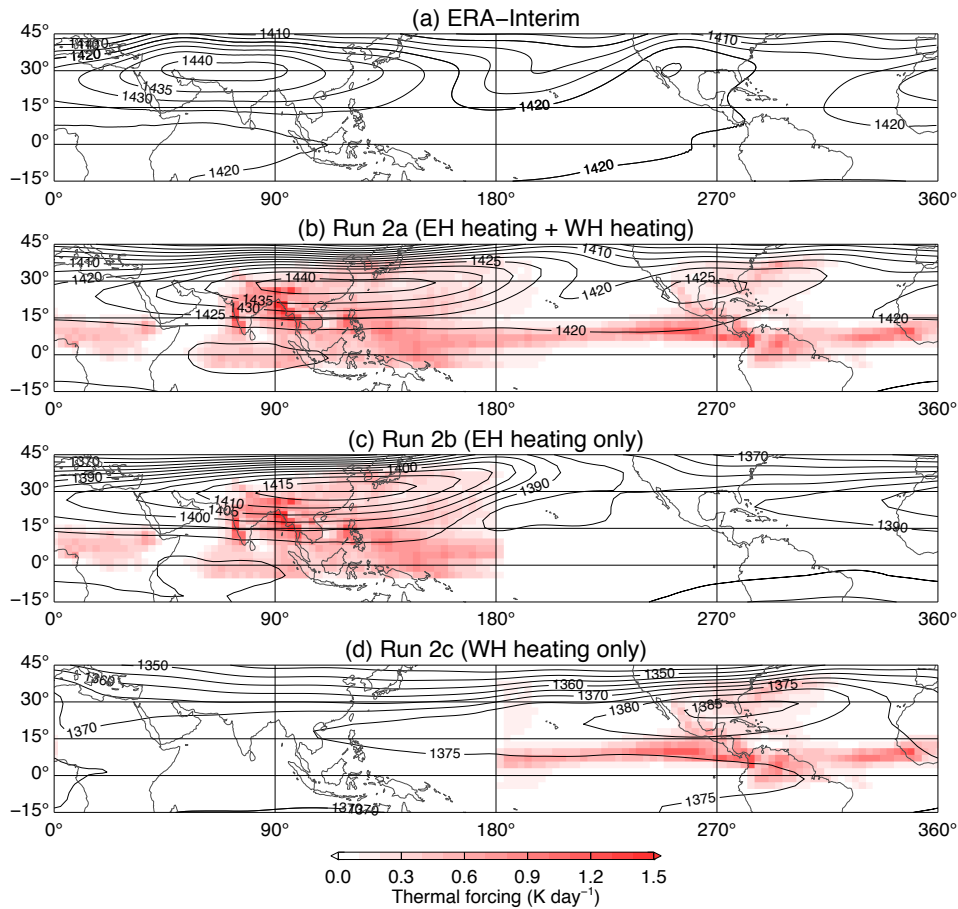
Figure 6.2: (a) ERA-Interim climatological July geopotential height *Z*. (b)–(d) Time-mean CAM *Z* (contours) for runs 2a–2c, respectively, with geographical distributions of TMPA-derived thermal forcing Q_{LH} (color). Both fields indicate values at 150 hPa. Contour interval of *Z* is 5 dam. The horizontal distribution of Q_{LH} is specified in Table 4.2. The model has no topography or land?ocean contrast, and the continents are shown only to provide a geographic reference.

6.1.2 Global Heating

The performance of the model when forced by heating in both the eastern and western hemispheres (run 2a) is assessed through comparisons with the ERA-Interim July climatology. Figure 6.1 shows selected time-mean, zonal-mean fields. CAM temperatures are high near the surface, which is typical for a dry GCM without surface energy fluxes (Figures 6.1a and 6.1b), but the discrepancy becomes smaller in the free troposphere (Figure 6.1c). The model produces a reason-

able structure for both summer and winter subtropical jets (Figures 6.1d and 6.1e), although the summer jet is somewhat strong compared to observations (31.2 m s^{-1} versus 21.8 m s^{-1}). The tropical easterlies are also stronger in the model than in observations, but the difference is modest (Figure 6.1f). The difference in jet strength can be attributed to a lack of other mechanisms of heat transport (Baker et al., 2017). The tropopause height in the deep tropics generally agrees well with observations. With a very weak stratospheric lapse rate (Figure 4.1c), the polar-night jet is absent in this model.

Figures 6.2a and 6.2b shows the observed and simulated geopotential height Z (contours) for the reanalysis and run 2a, respectively; the thermal forcing distribution Q_{LH} (color) is also shown in Figure 6.2b. Both quantities are plotted at 150 hPa. The simulation reproduces the size and magnitude of the anticyclones well compared to the reanalysis, although the center of the AMA is about 45° east of its observed position. The longitudinal bias of the center of NAMA is much smaller than for the AMA. Besides the eastward bias, the AMA is more zonally elongated in the model, which may be due to a somewhat large radiative relaxation time scale τ_r. The trough over the Pacific that separates the two anticyclones (near 150°W) is weaker in the simulation but is still noticeable.

Figure 6.3 compares meridional and zonal vertical sections of the time-mean horizontal wind structure through the centers of the AMA and NAMA. Zonal averages of u and meridional averages of v are computed over 45° sectors and 10° zones, respectively. Note the shift in longitude for the zonal section of the AMA in Figure 6.3d. For the AMA, the subtropical westerlies are stronger in the model, as expected from Figure 6.1e, but the difference of strength in the tropical easterlies is small (Figures 6.3a and 6.3c). The meridional wind in the AMA is slightly stronger in the model (Figures 6.3b and 6.3d). The vertical extent of the AMA is between 300 and 50 hPa and agrees well between the observations and simulation. For the NAMA, the simulation satisfactorily reproduces the magnitude and location of the subtropical jet (Figures 6.3e and 6.3g). Contrary to the AMA, the meridional wind in the AMA is slightly weaker in the model (Figures 6.3f and 6.3h). Also the NAMA does not extend as high as the AMA. Overall the simplified GCM is capable of reproducing
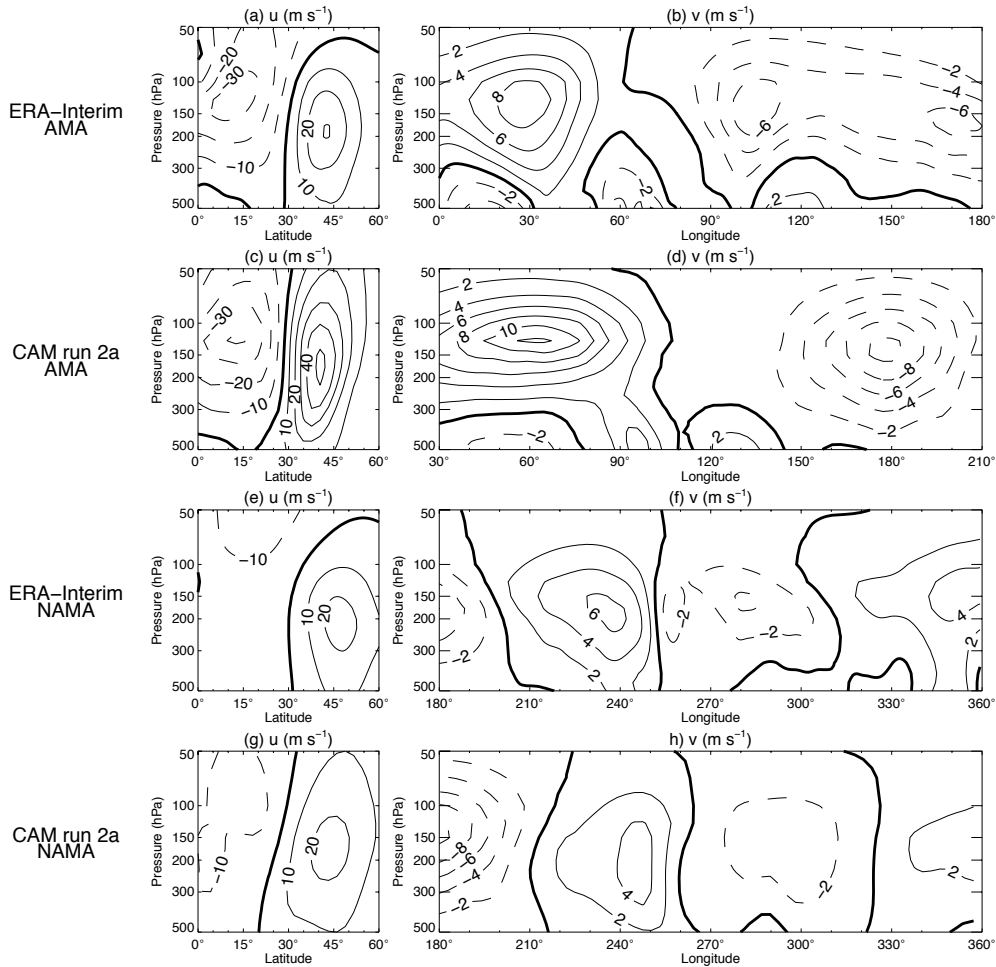
Figure 6.3: (left) Latitude–pressure cross sections of time-mean, longitudinal-mean zonal velocity u. (right) Longitude–pressure cross sections of time-mean, latitudinal-mean meridional velocity v. Only cross sections between 500 and 50 hPa are shown. Note that the longitude (latitude) ranges of observations and model used for averaging u (v) are different but the extents of longitude ($\Delta\lambda = 45°$) and latitude ($\Delta\phi = 10°$) are the same. Note also that the longitude range of (d) is shifted 30° eastward for better correspondence with observations. (a),(b) ERA-Interim climatological July u (0°–60°N, 45°–90°E) and v (25°–35°N, 0°–180°E). (c),(d) CAM u (0°–60°N, 90°–135°E) and v (20°–30°N, 30°E–150°W). (e),(f) ERA-Interim climatological July u (0°–60°N, 120°–75°W) and v (25°–35°N, 180°W–0°). (g),(h) CAM u (0°–60°N, 120°–75°W) and v (20°–30°N, 180°W–0°). Contour intervals of u and v are 10 m s^{-1} and 2 m s^{-1}, respectively (solid for positive values, dashed for negative values, and bold for zero).

the major features of both anticyclones with realistic amplitudes when forced by the observed, time-averaged, geographical distribution of latent heating.

50

The diabatic heating from the physics package in (4.1) consists of the radiative heating Q_R, convective heating Q_C, and latent heating Q_{LH}. The convective adjustment normally stabilizes the troposphere by transporting heat upward. Inside regions with abundant precipitation (e.g., monsoon regions), the heating is dominated by Q_R and Q_{LH}, and Q_C is very small by comparison. Inside dry regions (e.g., the Sahara), Q_{LH} and Q_C can have similar magnitudes but the total heating is still dominated by Q_R. Therefore, the overall contribution of convective heating within the forcing region is very small.

6.1.3   Hemispheric Heating

Experiment 2a provides the basis for analyzing the contributions to the forcing from individual geographical regions. The forcing is first divided into eastern- and western-hemisphere contributions (Figures 6.2c and 6.2d; runs 2b and 2c). The total heating in run 2a is equal to the sum of the heating in runs 2b and 2c (Table 4.2). The AMA is slightly weaker when the western-hemisphere heating is removed (Figure 6.2c). A deep trough is still distinct in the Pacific. Similarly, the NAMA is slightly weaker when the eastern-hemisphere heating is removed (Figure 6.2d). In runs 2b and 2c the westerlies are somewhat weaker than in run 2a. These experiments demonstrate that in the model the anticyclones are little affected by remote heat sources. That is, the anticyclones are primarily a response to nearby thermal forcing in their respective hemispheres, and there is no indication that the NAMA is a downstream response to the Asian monsoon circulation.

6.1.4   Partitioning the Western-Hemisphere Heating

Runs 2a–2c show that the NAMA is principally driven by latent heating in the western hemisphere. Runs 3a–3i are then used to determine the importance of heating in different longitude sectors and latitude zones within the western hemisphere. The heating is first partitioned into three 60° longitude sectors (WH1, WH2, and WH3) as defined in Figure 6.4. Figure 6.5 shows the longitudinal-mean precipitation in these three sectors. One eastern hemisphere sector (EH1) is shown for comparison. The maximum WH and EH precipitation rates are similar, but the WH sectors are dominated by the narrow ITCZ precipitation located between 0° and 15°N, while EH1
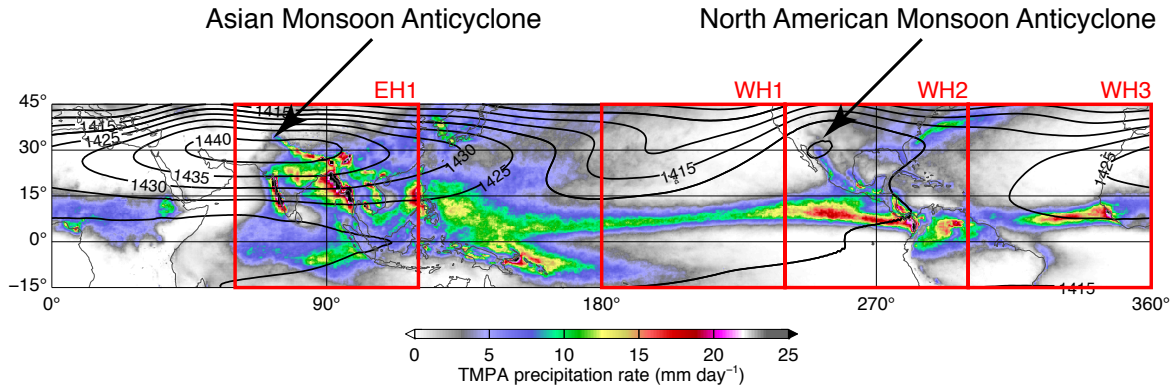
Figure 6.4: TMPA climatological July precipitation rate R (color) and ERA-Interim climatological July geopotential height Z at 150 hPa (contours; interval: 5 dam). The Asian and North American monsoon anticyclones are labeled and indicated by arrows. Four longitude sectors (EH1, WH1, WH2, WH3) of equal size are labeled and outlined in red. The longitudinal-mean precipitation of these sectors is examined in Figure 6.5.
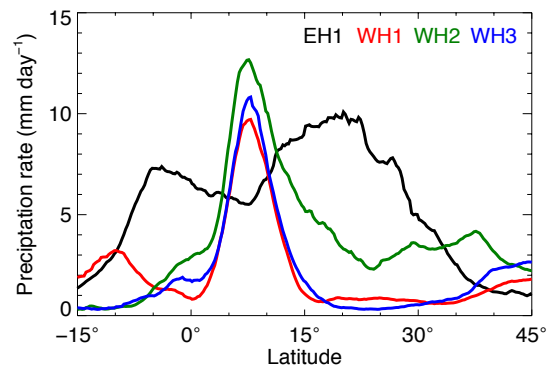
Figure 6.5: TMPA longitudinal-mean climatological July precipitation rate R of sectors EH1, WH1, WH2, and WH3 in color, as defined in Figure 6.4.

has a large amount of precipitation between about $10°$ and $40°$N. There is little subtropical precipitation in WH1 and WH3 (less than 1 mm day^{-1}), but there is a substantial amount of precipitation poleward of $15°$N in the middle sector, WH2.

Results for the three WH sectors simulations (runs 3a–3c) are shown in the top three panels of Figure 6.6. Note that the latitudinal extent of the heating is limited to be between $5°$S and $40°$N. The
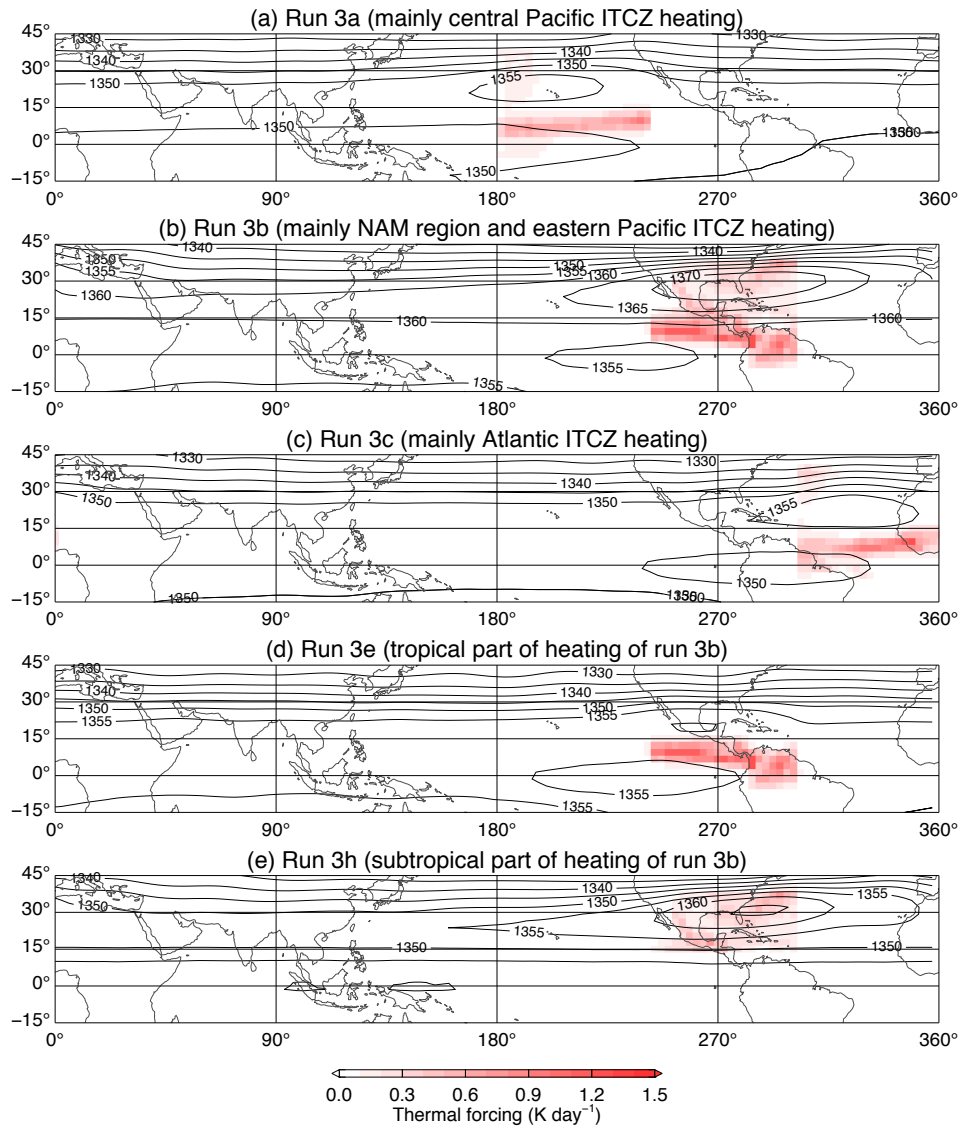
Figure 6.6: As in Figure 6.2 but for runs 3a–3c, 3e, and 3h.

total heating in run 3b (middle sector) comprises ∼51% of the total western-hemisphere heating in run 2c (Table 4.2), and it has substantially more precipitation in the subtropics than the other two runs. For runs 3a and 3c, which have heating primarily within the Pacific and Atlantic ITCZs, respectively, the subtropical response is weak. Run 3b, however, produces a substantial anticyclone in the subtropics.

To investigate the relative importance of the magnitude of the heating and its meridional distri-

bution, each longitude sector is divided at 15°N into tropical and subtropical latitude zones, giving six regions. Experiments 3d through 3i are carried out using heating from those individual regions. Runs 3d and 3f (not shown), which include only the tropical part of the heating from runs 3a and 3c, produce weak anticyclones similar to Figures 6.6a and 6.6c. Similarly, runs 3g and 3i, which have only a small amount of heating in the subtropics, produce weak anticyclones (not shown). In the middle sector, however, both runs 3e (tropical heating) and 3h (subtropical heating) produce a subtropical anticyclone (Figures 6.6d and 6.6e), with a much stronger response coming from the latter case. Note that although the response from the subtropical heating is larger, the total heating in the subtropical sector is only ∼62% of the tropical sector (Table 4.2). These two simulations suggest that the latitude of the heating plays a significant role in determining the strength of the anticyclone.

We note that precipitation over Mexico and the southern United States, along with the NAMA response in the UTLS, exhibits a northward propagation during late spring and early summer (Higgins et al., 1999). Run 3e resembles the early stage of the NAMA, with a weak anticyclone at a low latitude, while runs 3b and 3h, which are very similar, can be viewed as the mature stage of the NAMA. A closer look at the geographical distribution of the heating in these simulations suggests that the onset of the North American monsoon precipitation across different regions is intimately related to the northward propagation and development of the NAMA.

6.2   Response to the Idealized Forcing

6.2.1   Zonally-Elongated Heating

Although all three WH sectors have substantial precipitation in the deep tropics, only the heating in WH2, which also has substantial precipitation in the subtropics, produces a significant subtropical response. Experiments 3e and 3h show that, despite the large magnitude of forcing, the response to the tropical precipitation in WH2 is small; and the anticyclone in run 2c is produced primarily by subtropical heating. The preliminary experiments and these realistic forcing experiments suggest that the magnitude and latitude of the forcing are both important for controlling the strength

of anticyclones, which supports the Gill-type response (1.1). To explore this question in a simpler context, we use two different idealized horizontal distributions, as described in chapter 4.

The experiments in this section (group 4) investigate the role of the latitude of the heating in the atmospheric response using idealized zonally-elongated heating distributions. The total amount of heating is the same at all latitudes to isolate its effect in (1.1). The meridional profile of the heating is given by (4.5), with the meridional extent $\Delta\phi$ set to 15° which is comparable to the narrow extent of the ITCZ in the three WH sectors as seen in Figure 6.5.

Runs 4a–4e use a global zonally-symmetric heating distribution centered at different latitudes. As expected, zonally symmetric forcing does not produce a localized anticyclone, even if the forcing is located in the subtropics, so no results from these experiments are shown here.

Runs 4f–4j restrict the zonally-elongated heating to a 180° longitude sector centered at 90°W ($\Delta\lambda = 180°$ and $\lambda_0 = 90°$W), with the center latitude ϕ_0 ranging from 0° to 30°N in 7.5° increments (Table 4.3). The total amount of the heating is 25×10^{19} J day^{-1}, which is similar to the total amount of the tropical part between 0° and 15°N of the western-hemisphere heating in run 2c (or the sum of the tropical heating between 0° and 15°N in runs 3d–3f). The magnitude of the thermal forcing is adjusted in each run to keep the total amount of heating constant.

Figure 6.7 shows the results from experiments 4g and 4i. The quantity displayed is the zonally asymmetric part of the atmospheric response $Z^* = Z - [Z]$, where Z is the time-mean geopotential height at 150 hPa and square brackets indicate the zonal average of Z. The magnitude of the anticyclone Z^*_{max} is defined as the maximum value of Z^* outside the tropics. Run 4g, with $\phi_0 = 7.5°$N, resembles the ITCZ precipitation in Figure 6.5 (Figure 6.7a). The response to this forcing in the subtropics and extratropics is weak. The response in the equatorial channel is even weaker. When the heating is centered at the equator, the responses are fairly similar although the equatorial channel response to the east of the forcing is slightly stronger (not shown). Differences of the responses between run 4g and Gill's solution can be attributed to differences in the basic state and in the shape of the heating distribution. The heating in Gill's model has a larger meridional extent than the heating in run 4g. Here, narrow heating confined to the deep tropics leads to a smaller meridional
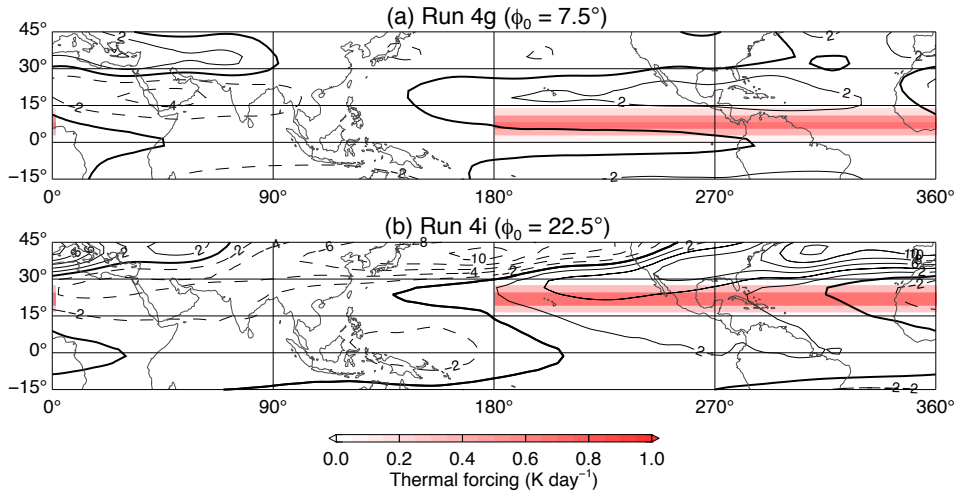
Figure 6.7: Time-mean geopotential height anomaly Z^* (contours) and geographical distributions of zonally-elongated heating Q_{LH} (color) for runs (a) 4g and (b) 4i. Both fields indicate values at 150 hPa. Contour interval of Z^* is 2 dam (solid for positive values, dashed for negative values, and bold for zero). Note the change of the color-bar scale from Figures 6.2 and 6.6.

velocity due to the weaker Coriolis effect and vortex stretching mechanism at lower latitudes (cf. Figure 3 of Phlips and Gill (1987)). The responses in the tropics and subtropics are still weak when the heating moves to $\phi_0 = 15°$ (not shown). The extratropical response becomes distinct when the heating moves to $\phi_0 = 22.5°$N in run 4i (Figure 6.7b). A very zonally-elongated anticyclone covers the whole western hemisphere. The response is similar to run 4i when the heating moves to $\phi_0 = 30°$N (not shown).

6.2.2 Compact Regional Heating

Because narrow and zonally-elongated heating in the deep tropics produces little response in the subtropics, we next consider the response to more compact regional heating. For this we use the idealized heating distribution given by (4.6) with a zonal extent $\Delta\lambda$ of 60° and a meridional extent $\Delta\phi$ of 30°. The meridional extent is set to roughly match the extent of the precipitation if the ITCZ peak is subtracted from the profile in WH2 (Figure 6.5). Runs 5a–5e examine the effect of the latitude of the heat source by varying the center latitude ϕ_0 from 0° to 20°N in 5° increments

56

(Table 4.3). The total amount of the heating is 6×10^{19} J day^{-1}, which is less than one quarter of the zonally-elongated heating in the previous subsection. The magnitude of heating is chosen so that the sum of the regional heating from runs 5a–5e and the zonally-elongated heating from runs 4f–4j is close to the total amount of western-hemisphere heating between 0° and 30°N in run 2c. Run 5d ($\phi_0 = 15°$N) resembles the regional precipitation in WH2; run 5e ($\phi_0 = 20°$N) better matches the geographic distribution, while underrepresenting the magnitude of the precipitation in the Asian sector EH1 (Figure 6.5).

Figure 6.8 shows the eddy response Z^* to the regional heating at different latitudes. Forcing at the equator (run 5a), excites weak extratropical responses to the north (Figure 6.8a). As the forcing is shifted poleward, the responses in the tropical channel to the west and in the extratropics strengthen somewhat (Figure 6.8b). For ϕ_0 between 10° and 20°N (Figures 6.8c–e), the forcing produces a response in both tropics and subtropics, resulting in a quadrupole structure with anomalous westerlies east of the heat source and easterlies west of the heat source. The locations of the NAMA in runs 5c–5e are similar to run 3b (Figures 6.8c–e), while the maximum response to the regional forcing increases substantially as ϕ_0 moves from 15°N to 20°N. With a constant amount of latent heating, experiment 5 shows that the response strengthens as the heating moves poleward and f increases. This suggests that the AMA is stronger than the NAMA because of both the larger amount of latent heating in the eastern hemisphere (Figure 6.5) and the more poleward position of the intense heating outside the deep tropics (Figure 6.8e).

Compared to the zonally-elongated forcing experiments, a distinct extratropical response appears for a lower ϕ_0 with the compact forcing. This is because the meridional extent of the compact heating is wider (30° versus 15°), the heating has an effect in the subtropics while the center is still in the deep tropics. Figures 6.7 and 6.8 show that when the length of the forcing region decreases, the zonal extent of the extratropical response also decreases. For example, other than the elongated anticyclone, a wavenumber one response is clearly seen in the eastern hemisphere due to the 180° longitude heating (Figure 6.7b). It suggests that similar zonal scales of the heating region produce similar zonal extents of the extratropical response. It implies that the AMA covers a much
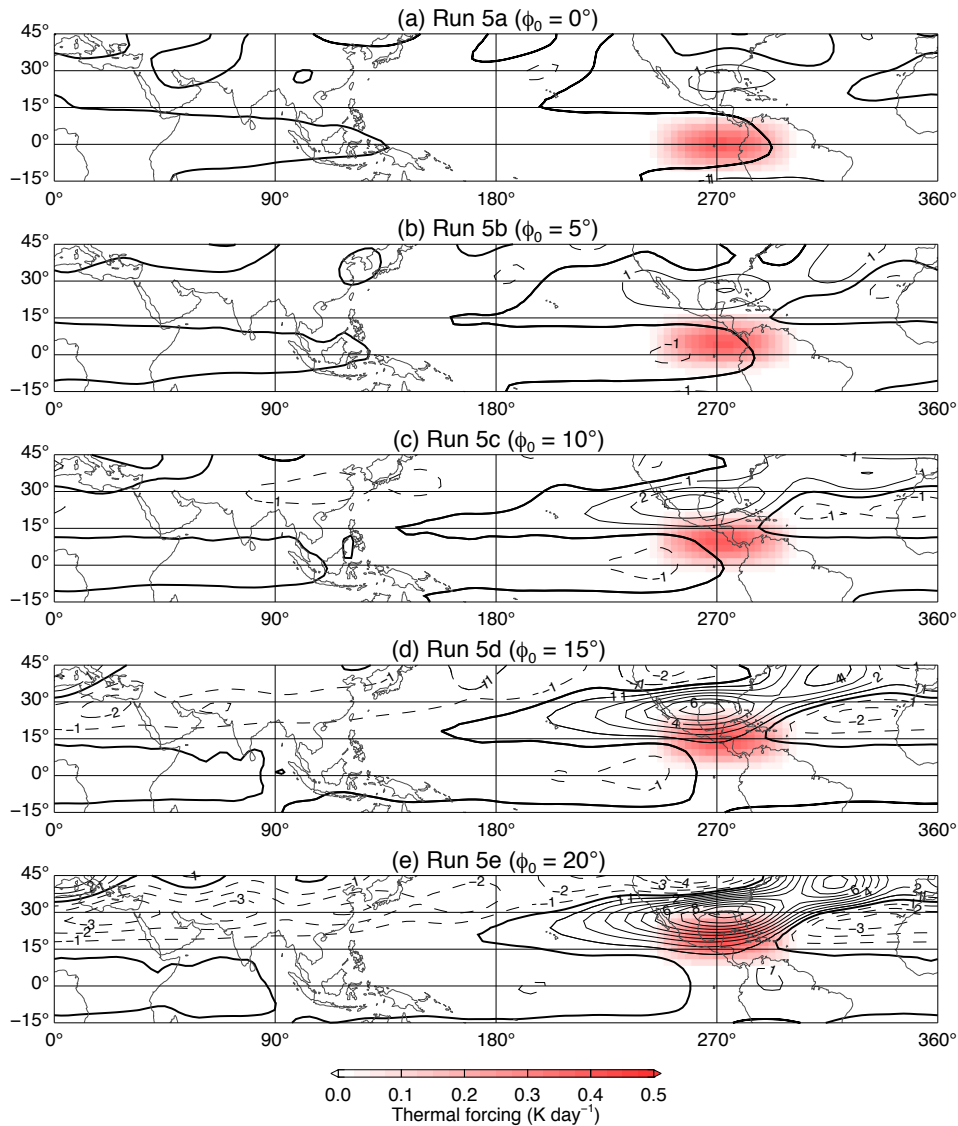
Figure 6.8: As in Figure 6.7 but for runs (a) 5a–(e) 5e with the geographical distributions of compacted regional heating Q_{LH} (color). Contour interval of Z^* is 1 dam (solid for positive values, dashed for negative values, and bold for zero). Note the change of the color-bar scale from Figures 6.2, 6.6, and 6.7.

larger area than the NAMA because the zonal extent of the precipitation region in the *subtropics* of the eastern hemisphere is much larger than the analogous zonal extent in the western hemisphere (Figure 6.4).

Experiments 1 through 6 use T42L30 resolution. It has been reported that increasing the number of vertical levels could improve the simulation of Asian monsoon in the UTLS region in the
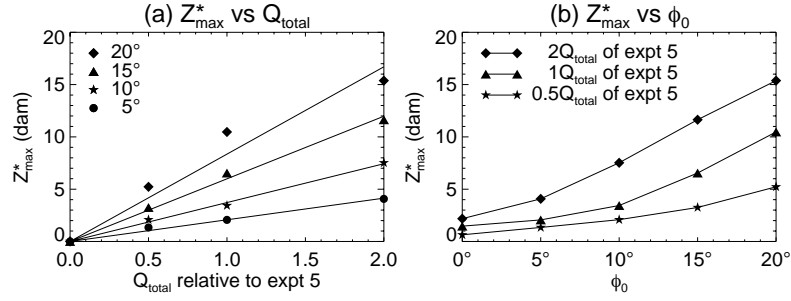
Figure 6.9: (a) Linear least squares fits of maximum time-mean geopotential height anomaly Z^*_{max} at 150 hPa with the intercept forced to be zero as a function of the total amount of heating Q_{total} relative to experiment 5 for selected center latitudes of the heating ϕ_0. (b) Z^*_{max} as a function of ϕ_0 for runs 5a–5e, 6a–6e ($0.5Q_{total}$ of experiment 5), and 6f–6j ($2Q_{total}$ of experiment 5). Scalings of Q_{total} are labeled (see also Table 4.3).

comprehensive version of the CESM (Wang et al., 2018). To test the sensitivity of the model to changes in both horizontal and vertical resolution, additional runs were carried out with higher horizontal resolution (runs 7a–7e at T85L30) and higher vertical resolution (runs 7f–7j at T42L60). In both cases the results do not change significantly from the T42L30 runs (not shown).

6.2.3 Linearity of the Response

The linearity of the atmospheric response is evaluated by repeating runs 5a–5e with the heating scaled by factors of 0.5 (runs 6a–6e) and 2 (runs 6f–6j). Details of the numerical experiments are given in Table 4.3. Figure 6.9a shows the strength of the anticyclone as a function of the total amount of forcing Q_{total} relative to experiment 5. The strength of the response is measured by the maximum geopotential height anomaly Z^*_{max} of the anticyclone. We fit the data points for each center latitude of forcing ϕ_0 using a linear least squares fit with the intercept forced to be zero. For a fixed value of ϕ_0, the amplitude of the response varies nearly linearly in relation to the magnitude of the heating within the range of heating values examined.

Figure 6.9b shows the strength of the anticyclone as a function of ϕ_0 for the same three sets of experiments. When the forcing is close to the equator, the response is weak. As the forcing shifts poleward, the response in increases somewhat nonlinearly as a function of latitude. This could be

in part a result of the nonlinear meridional profile of the heating. That is, the amount of heating in the subtropics increases nonlinearly as the center of the heating shifts poleward. If, however, the atmospheric response is plotted as a function of the total heating poleward of 15°N rather than ϕ_0 (not shown), the response remains nonlinear. This suggests that the nonlinearity of the response is not simply a result of the nonlinear meridional profile of the heating in (4.6).

7. DISCUSSION AND CONCLUSIONS[1]

Previous interpretations of the behavior of the Asian monsoon anticyclone are based primarily on analysis methods that allow only a single circulation center within the anticyclone at a given time (e.g., Zhang et al., 2002). This approach gives the impression that the AMA has two preferred centers, over Iran and the Tibetan Plateau, with transitions between those two states. Pan et al. (2016) suggested that two new modes should be included: a double-center mode and a longitudinally-elongated mode. These methods, however, do not allow for other transient behavior such as eddy shedding. In contrast, the method used here allows multiple simultaneous sub-vortices within the AMA. In addition, the locations of sub-vortices are tracked over time, which provides additional information about the evolution of the AMA over the warm season.

The analysis presented here reveals that two or more distinct persistent sub-vortices exist simultaneously within the AMA $\sim 75\%$ of the time. These sub-vortices often have similar strength. The preferred locations of the sub-vortices lie over Iran, the Tibetan Plateau, and the western Pacific Ocean (the Bonin High). The Iranian and Tibetan Highs often simultaneously and drift eastward or westward, so the distinct modes that appear in a single-center analysis merge into a broad peak in this analysis (Figure 5.4a). In addition, the Bonin High is clearly revealed as a distinct anticyclonic circulation center. Because it is generally weaker than the two continental circulation centers, it is rarely identified by single-center methods.

Time-longitude plots of sub-vortex locations reveal several types of behavior, including (1) splitting of a single vortex into two vortices; (2) merger of two vortices into a single vortex; (3) vortex shedding in the eastward direction; (4) vortex shedding in the westward direction; and (5) formation, movement, and dissipation of a vortex (Figure 5.1). The number and locations of sub-vortices evolve continuously on synoptic timescales. Eddy-shedding events occur but are not common. Eastward eddy-shedding events are more common than westward eddy-shedding events, as

---

[1]Part of this chapter is reprinted with permission from 'Forcing of the Upper-Tropospheric Monsoon Anticyclones.' by L. W. Siu and K. P. Bowman, 2019. J. Atmos. Sci., 76, 1937–1954, Copyright 2019 by American Meteorological Society.

indicated by the low frequency of vortex centers west of the 30°E. Unlike tropical cyclones, binary interactions, such as the Fujiwhara effect (i.e., mutual orbiting of two vortices), are not seen in the Asian monsoon anticyclone (Fujiwhara, 1921, 1923, 1931). This may be due to the strong confinement of the AMA between the subtropical jet and the tropical easterly jet and the limited space for two sub-vortices to rotate with each other.

There are limits to the present analysis determined by the resolution and quality of the meteorological analysis and the fundamental scales (smoothness) of the atmospheric flow. Additionally, the analysis method uses the Montgomery streamfunction Ψ to locate vortex centers, but the flow is not in exact balance, so Ψ is not a perfect indicator of where the instantaneous center of rotation is located. Also the half-width of the search window sets a lower limit on the size of sub-vortices that can be detected. This means that it is not possible to observe vortex splitting, merger, or other interactions when vortices are very close to one another, but only after they have separated sufficiently to be distinguished from each other. While the difference between vortex splitting and eddy shedding is not clearly defined in the literature, we define an eddy-shedding event to be when the eddy crosses 0° or 180°E for the case of the AMA. With this definition an eddy-shedding event signifies long-range atmospheric transport from the Eastern to the Western Hemisphere. Note that our definition may give different results compared to other analyses. Fadnavis et al. (2018) defined a shedding event to be the separation of low PV area ($<$ 1 PVU) from the main circulation. They found that it occurs more frequently over western Africa ($\sim$ 68%) than the western Pacific ($\sim$ 25%). Finally, the flow is quite complex and multiple types of behavior may happen at the same time, which can make classification difficult.

The transitions between states with one to three (or more) sub-vortices within the AMA play an important role in stirring the air in the interior of the anticyclone. These transitions are associated with the appearance and disappearance of hyperbolic regions between the sub-vortices, which can be identified by the *M* diagnostics. When a single vortex splits into two temporarily isolated vortices that then re-merge, air that was originally in compact patches is stretched and stirred into extended filaments (Figures 5.6 and 5.7). The result is efficient stirring of the air inside the anticyclone, which
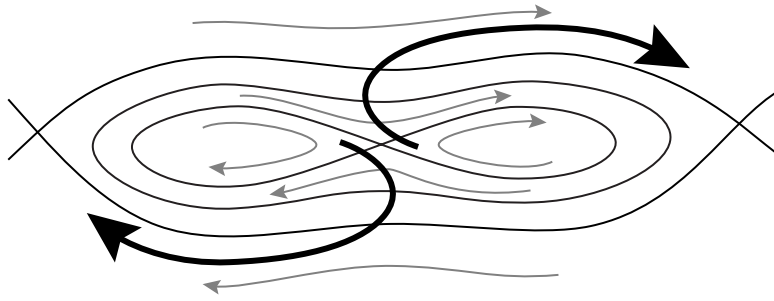
Figure 7.1: Transport pathways for air leaving the anticyclone when two vortices are present. Thin black lines represent instantaneous streamlines. Thin gray arrows indicate the direction of the flow. Heavy black arrows show the paths taken by air exiting the hyperbolic region between the two vortices.

is similar to the stirring seen in the idealized model of Aref (1984). As was shown in Figures 5.8 and 5.9, patches of air exiting the vortex do so through lobes associated with hyperbolic regions. In the case that has been examined in detail, air that forms a coherent eastward propagating eddy is not pinched off the eastern end of the AMA, as was suggested in Figure 1.3, but instead comes from filaments exported from the anticyclone via the lobes associated with the hyperbolic region between the two sub-vortices. This eddy moves across the Pacific and reach the Pacific coast of the United States in around ten days. Westward shedding events are uncommon, but the example in Figure 5.9 is also associated with the hyperbolic region. These transport pathways are illustrated schematically in Figure 7.1.

This study is fundamentally kinematic and, as such, does not directly address the dynamical reasons for the unsteady behavior of the Asian monsoon anticyclone. The appearance, disappearance, and motion of sub-vortices may be due to spatial or temporal variability of the latent heat release that drives the formation of the anticyclone, to orographic forcing, to internal nonlinearity of the flow within the anticyclone, or to external forcing by extratropical Rossby waves propagating along the subtropical jet or instability of the jet itself. Hsu and Plumb (2000) studied the effect of asymmetry by imposing mean wind or PV gradient to a thermally forced anticyclonic circulation in a shallow water model and showed that eddies can be periodically shed under sufficiently strong asymmetry.

Amemiya and Sato (2018) developed a nonlinear shallow water model that exhibits more realistic westward shedding and vortex splitting by including a latitude-dependent mean depth and varying the vertical gradient of the diabatic heating. However, these models do not exhibit eastward shedding which is observed in the data. Additional studies are needed to understand the dynamics of the different types of the vortex behavior.

The origin and dynamics of the upper tropospheric North American monsoon anticyclone are investigated through numerical experiments with an idealized general circulation model and comparisons with observational analyses. The analysis focuses on the time-averaged response of the atmosphere. The model uses a simplified physics package based on Held and Suarez (1994) that relaxes the temperature to a prescribed zonally-symmetric basic state. To simulate a more realistic tropical circulation, the physical parameterizations and basic state are modified somewhat from HS94 according to Schneider and Walker (2006); and an explicit dry convection scheme is included. The model is forced by a steady diabatic heat source based on TMPA precipitation data or prescribed from idealized heating distributions. Significant approximations in the idealized model include the absence of topography, land-sea contrast, and temporal variations of the forcing. These effects are partially compensated by adjusting the magnitude of the thermal forcing. The model uses a constant vertical heating profile throughout the region where heating is applied and ignores heating outside of the tropics and northern hemisphere subtropics. Experiments with increased horizontal and vertical resolution (T85L30 and T42L60) show that the simulations are not sensitive to either horizontal or vertical resolution.

The model is first tuned to give a realistic representation of the boreal summer upper tropospheric circulation, including the AMA, NAMA, and the mid-Pacific trough, using a realistic geographical distribution of diabatic heating based on the observed TMPA time-mean precipitation. To produce a realistic zonal-mean circulation, the latent heating is scaled to 59% of its observed value. This heating distribution is partitioned geographically in various ways, and the response to each individual region is examined. When the heating is turned off in either the eastern or western hemisphere, the anticyclone in that hemisphere disappears, while the anticyclonic circulation in the

64

other hemisphere slightly weakens. This demonstrates that the AMA and NAMA are fundamentally responses to diabatic heating within their respective hemispheres, and the NAMA in particular is not a downstream wave response to Asian monsoonal heating. During the warm season the majority of the precipitation in the western hemisphere falls in a narrow zone between about 5° and 15°N within the Atlantic and Pacific ITCZs and across the northern part of South America. The NAMA, however, is primarily a response to heating poleward of 15°N in the longitude sector between 60° and 120°W, which includes the northern part of Central America, Mexico, the southern United States, the Caribbean Sea, and the Gulf of Mexico. This demonstrates the importance of the latitude of the heating to the response.

To explore the atmospheric response to the shape and location of the heating, the model is forced with idealized heating distributions that represent either zonally-elongated (ITCZ-like) or compact regional precipitation features. When the zonally-elongated heating is placed near the equator, the response in the extratropics is weak. The extratropical response is significant only when the heating is located outside the deep tropics. The response to a compact heating distribution depends on the latitude of the heating as well. An extratropical response is evident when the heating is centered poleward of 10°N, and the extent of the response is more localized compared to the zonally-elongated forcing. These experiments support the conclusion that the AMA is stronger than the NAMA because of both the heavier precipitation in the eastern hemisphere *and* the location of the intense precipitation at higher latitudes over Asia compared to North America. Compared to the zonally-elongated heating, the compact heating is shorter in the zonal direction and wider in the meridional direction. The numerical experiments indicate that the longitudinal extent of the AMA is much larger than the NAMA in part because the zonal extent of the subtropical precipitation in the eastern hemisphere is greater than in the western hemisphere.

The linearity of the atmospheric response of the idealized forcing experiments is examined by varying the magnitude of the heating. To a good approximation the strength of the anticyclone is linearly proportional to the magnitude of the applied heating, but for a fixed magnitude of heating the response depends nonlinearly on the latitude of the heating.

The model results support the idea that the AMA and NAMA are largely independent of one another, being forced primarily by diabatic heating in their respective hemispheres. That is, both anticyclones are Matsuno–Gill type responses. The differences in the amplitude and zonal extent of the AMA and NAMA are due in part to the total amount and zonal distribution of heating in each hemisphere, but are primarily a result of the different meridional distributions of heating in the two hemispheres.

REFERENCES

Adams, D. K., and A. C. Comrie, 1997: The North American Monsoon. *Bull. Amer. Meteor. Soc.*, **78 (10)**, 2197–2213, doi:10.1175/1520-0477(1997)078<2197:TNAM>2.0.CO;2.

Amemiya, A., and K. Sato, 2018: A two-dimensional dynamical model for the subseasonal variability of the Asian monsoon anticyclone. *J. Atmos. Sci.*, **75 (10)**, 3597–3612, doi:10.1175/JAS-D-17-0208.1.

Aref, H., 1984: Stirring by chaotic advection. *J. Fluid Mech.*, **143**, 1–21, doi:10.1017/S0022112084001233.

Baker, A. K., T. J. Schuck, F. Slemr, P. van Velthoven, A. Zahn, and C. A. M. Brenninkmeijer, 2011: Characterization of non-methane hydrocarbons in Asian summer monsoon outflow observed by the CARIBIC aircraft. *Atmos. Chem. Phys.*, **11 (2)**, 503–518, doi:10.5194/acp-11-503-2011.

Baker, H. S., T. Woollings, and C. Mbengue, 2017: Eddy-driven jet sensitivity to diabatic heating in an idealized GCM. *J. Climate*, **30 (16)**, 6413–6431, doi:10.1175/JCLI-D-16-0864.1.

Barlow, M., S. Nigam, and E. H. Berbery, 1998: Evolution of the North American monsoon system. *J. Climate*, **11 (9)**, 2238–2257, doi:10.1175/1520-0442(1998)011<2238:EOTNAM>2.0.CO;2.

Bergman, J. W., F. Fierli, E. J. Jensen, S. Honomichl, and L. L. Pan, 2013: Boundary layer sources for the Asian anticyclone: Regional contributions to a vertical conduit. *J. Geophys. Res. Atmos.*, **118 (6)**, 2560–2575, doi:10.1002/jgrd.50142.

Bowman, K. P., 1993: Large-scale isentropic mixing properties of the Antarctic polar vortex from analyzed winds. *J. Geophys. Res. Atmos.*, **98 (D12)**, 23 013–23 027, doi:10.1029/93JD02599.

Bowman, K. P., and G. D. Carrie, 2002: The mean-meridional transport circulation of the troposphere in an idealized GCM. *J. Atmos. Sci.*, **59 (9)**, 1502–1514, doi:10.1175/1520-0469(2002)059<1502:TMMTCO>2.0.CO;2.

Brunamonti, S., and Coauthors, 2018: Balloon-borne measurements of temperature, water vapor, ozone and aerosol backscatter on the southern slopes of the Himalayas during StratoClim 2016–2017. *Atmos. Chem. Phys.*, **18 (21)**, 15 937–15 957, doi:10.5194/acp-18-15937-2018.

Chao, W. C., and B. Chen, 2001: The origin of monsoons. *J. Atmos. Sci.*, **58 (22)**, 3497–3507, doi:10.1175/1520-0469(2001)058<3497:TOOM>2.0.CO;2.

Chen, P., 1995: Isentropic cross-tropopause mass exchange in the extratropics. *J. Geophys. Res. Atmos.*, **100 (D8)**, 16 661–16 673, doi:10.1029/95JD01264.

Chen, P., M. P. Hoerling, and R. M. Dole, 2001: The Origin of the Subtropical Anticyclones. *J. Atmos. Sci.*, **58 (13)**, 1827–1835, doi:10.1175/1520-0469(2001)058<1827:TOOTSA>2.0.CO;2.

Chen, T.-C., 2003: Maintenance of summer monsoon circulations: A planetary-scale perspective. *J. Climate*, **16 (12)**, 2022–2037, doi:10.1175/1520-0442(2003)016<2022:MOSMCA>2.0.CO;2.

Dao, S.-Y., and L.-S. Chen, 1957: The structure of general circulation over continent of Asia in summer. *J. Meteor. Soc. Japan*, **35A**, 215–229, doi:10.2151/jmsj1923.35A.0_215.

Dao, S.-Y., and F.-K. Chu, 1964: The 100-mb flow patterns in Southern Asia in summer and its relation to the advance and retreat of the West-Pacific subtropical anticyclone over the far east. *Acta Meteor. Sinica*, **34 (4)**, 387–396, doi:10.11676/qxxb1964.039.

de la Cámara, A., A. M. Mancho, K. Ide, E. Serrano, and C. R. Mechoso, 2012: Routes of transport across the Antarctic polar vortex in the southern spring. *J. Atmos. Sci.*, **69 (2)**, 741–752, doi:10.1175/JAS-D-11-0142.1.

de la Cámara, A., C. R. Mechoso, A. M. Mancho, E. Serrano, and K. Ide, 2013: Isentropic transport within the Antarctic polar-night vortex: Rossby wave breaking evidence and Lagrangian structures. *J. Atmos. Sci.*, **70 (9)**, 2982–3001, doi:10.1175/JAS-D-12-0274.1.

Dee, D. P., and Coauthors, 2011: The ERA-Interim reanalysis: Configuration and performance of the data assimilation system. *Quart. J. Roy. Meteor. Soc.*, **137 (656)**, 553–597, doi:10.1002/qj.828.

DeMaria, M., 1985: Linear response of a stratified tropical atmosphere to convective forcing. *J. Atmos. Sci.*, **42 (18)**, 1944–1959, doi:10.1175/1520-0469(1985)042<1944:LROAST>2.0.CO;2.

Dethof, A., A. O'Neill, J. M. Slingo, and H. G. J. Smit, 1999: A mechanism for moistening the lower stratosphere involving the Asian summer monsoon. *Quart. J. Roy. Meteor. Soc.*, **125 (556)**, 1079–1106, doi:10.1002/qj.1999.49712555602.

Douglas, M. W., R. A. Maddox, K. Howard, and S. Reyes, 1993: The Mexican monsoon. *J. Climate*, **6 (8)**, 1665–1677, doi:10.1175/1520-0442(1993)006<1665:TMM>2.0.CO;2.

Dunkerton, T. J., 1995: Evidence of meridional motion in the summer lower stratosphere adjacent to monsoon regions. *J. Geophys. Res. Atmos.*, **100 (D8)**, 16 675–16 688, doi:10.1029/95JD01263.

ECMWF, 2009: ERA-Interim project. National Center for Atmospheric Research Computational and Information Systems Laboratory Research Data Archive, accessed 1 January 2019, https://doi.org/10.5065/D6CR5RD9.

Enomoto, T., B. J. Hoskins, and Y. Matsuda, 2003: The formation mechanism of the Bonin high in August. *Quart. J. Roy. Meteor. Soc.*, **129 (587)**, 157–178, doi:10.1256/qj.01.211.

Fadnavis, S., C. Roy, R. Chattopadhyay, C. E. Sioris, A. Rap, R. Müller, K. R. Kumar, and R. Krishnan, 2018: Transport of trace gases via eddy shedding from the Asian summer monsoon anticyclone and associated impacts on ozone heating rates. *Atmos. Chem. Phys.*, **18 (15)**, 11 493–11 506, doi:10.5194/acp-18-11493-2018.

Flohn, H., 1950: Studien zur allgemeinen zirkulation der atmosphäre. *Ber. Dtsch. Wetterdienstes U.S. Zone*, **18**, 1–52.

Fujiwhara, S., 1921: The natural tendency towards symmetry of motion and its application as a principle in meteorology. *Quart. J. Roy. Meteor. Soc.*, **47 (200)**, 287–292, doi:10.1002/qj.49704720010.

Fujiwhara, S., 1923: On the growth and decay of vortical systems. *Quart. J. Roy. Meteor. Soc.*, **49 (206)**, 75–104, doi:10.1002/qj.49704920602.

Fujiwhara, S., 1931: Short note on the behavior of two vortices. *Proc. Phys.-Math. Soc. Japan*, **13 (3)**, 106–110, doi:10.11429/ppmsj1919.13.3_106.

Gadgil, S., 2003: The Indian monsoon and its variability. *Annu. Rev. Earth Planet. Sci.*, **31 (1)**, 429–467, doi:10.1146/annurev.earth.31.100901.141251.

Garny, H., and W. J. Randel, 2013: Dynamic variability of the Asian monsoon anticyclone observed in potential vorticity and correlations with tracer distributions. *J. Geophys. Res. Atmos.*, **118 (24)**, 13 421–13 433, doi:10.1002/2013JD020908.

Gill, A. E., 1980: Some simple solutions for heat-induced tropical circulation. *Quart. J. Roy. Meteor. Soc.*, **106 (449)**, 447–462, doi:10.1002/qj.49710644905.

Gill, A. E., 1982: *Atmosphere-Ocean Dynamics*. Academic Press, 662 pp.

Gottschaldt, K.-D., and Coauthors, 2018: Dynamics and composition of the Asian summer monsoon anticyclone. *Atmos. Chem. Phys.*, **18 (8)**, 5655–5675, doi:10.5194/acp-18-5655-2018.

Held, I. M., and M. J. Suarez, 1994: A proposal for the intercomparison of the dynamical cores of atmospheric general circulation models. *Bull. Amer. Meteor. Soc.*, **75 (10)**, 1825–1830, doi:10.1175/1520-0477(1994)075<1825:APFTIO>2.0.CO;2.

Higgins, R. W., Y. Chen, and A. V. Douglas, 1999: Interannual variability of the North American warm season precipitation regime. *J. Climate*, **12 (3)**, 653–680, doi:10.1175/1520-0442(1999)012<0653:IVOTNA>2.0.CO;2.

Higgins, R. W., K. C. Mo, and Y. Yao, 1998: Interannual variability of the U.S. summer precipitation regime with emphasis on the southwestern monsoon. *J. Climate*, **11 (10)**, 2582–2606, doi:10.1175/1520-0442(1998)011<2582:IVOTUS>2.0.CO;2.

Higgins, R. W., Y. Yao, and X. L. Wang, 1997: Influence of the North American monsoon system on the U.S. summer precipitation regime. *J. Climate*, **10 (10)**, 2600–2622, doi:10.1175/1520-0442(1997)010<2600:IOTNAM>2.0.CO;2.

Highwood, E. J., and B. J. Hoskins, 1998: The tropical tropopause. *Quart. J. Roy. Meteor. Soc.*, **124 (549)**, 1579–1604, doi:10.1002/qj.49712454911.

Holton, J. R., 2004: *An Introduction to Dynamic Meteorology*. 4th ed., Academic Press, 535 pp.

Holton, J. R., P. H. Haynes, M. E. McIntyre, A. R. Douglass, R. B. Rood, and L. Pfister, 1995: Stratosphere–troposphere exchange. *Rev. Geophys.*, **33 (4)**, 403–439, doi:10.1029/95RG02097.

Homeyer, C. R., and K. P. Bowman, 2013: Rossby wave breaking and transport between the tropics and extratropics above the subtropical jet. *J. Atmos. Sci.*, **70 (2)**, 607–626, doi:10.1175/JAS-D-12-0198.1.

Homeyer, C. R., K. P. Bowman, L. L. Pan, E. L. Atlas, R.-S. Gao, and T. L. Campos, 2011: Dynamical and chemical characteristics of tropospheric intrusions observed during START08. *J. Geophys. Res. Atmos.*, **116 (D6)**, doi:10.1029/2010JD015098.

Hoskins, B. J., and M. J. Rodwell, 1995: A model of the Asian summer monsoon. Part I: The global scale. *J. Atmos. Sci.*, **52 (9)**, 1329–1340, doi:10.1175/1520-0469(1995)052<1329:AMOTAS>2.0.CO;2.

Hovmöller, E., 1949: The trough-and-ridge diagram. *Tellus*, **1 (2)**, 62–66, doi:10.1111/j.2153-3490.1949.tb01260.x.

Hsu, C. J., and R. A. Plumb, 2000: Nonaxisymmetric thermally driven circulations and upper-tropospheric monsoon dynamics. *J. Atmos. Sci.*, **57 (9)**, 1255–1276, doi:10.1175/1520-0469(2000)057<1255:NTDCAU>2.0.CO;2.

Huffman, G. J., and D. T. Bolvin, 2018: TRMM and other data precipitation data set documentation. Tech. rep., NASA Goddard Space Flight Center, 46 pp. [Available online at https://pmm.nasa.gov/sites/default/files/document_files/3B42_3B43_doc_V7_180426.pdf.].

Huffman, G. J., and Coauthors, 2007: The TRMM Multisatellite Precipitation Analysis (TMPA): Quasi-global, multiyear, combined-sensor precipitation estimates at fine scales. *J. Hydrometeor.*, **8 (1)**, 38–55, doi:10.1175/JHM560.1.

Irving, D., 2016: A minimum standard for publishing computational results in the weather and climate sciences. *Bull. Amer. Meteor. Soc.*, **97 (7)**, 1149–1158, doi:10.1175/BAMS-D-15-00010.1.

Jiang, X., and N.-C. Lau, 2008: Intraseasonal Teleconnection between North American and Western North Pacific Monsoons with 20-Day Time Scale. *J. Climate*, **21 (11)**, 2664–2679, doi:10.1175/2007JCLI2024.1.

Koteswaram, P., 1958: The easterly jet stream in the tropics. *Tellus*, **10 (1)**, 43–57, doi:10.3402/tellusa.v10i1.9220.

Koteswaram, P., and N. S. B. Rao, 1963: The structure of the Asian summer monsoon. *Aust. Meteor. Mag.*, **42**, 35–56.

Krishnamurti, T. N., 1971: Observational study of the tropical upper tropospheric motion field during the Northern Hemisphere summer. *J. Appl. Meteor.*, **10 (6)**, 1066–1096, doi:10.1175/1520-0450(1971)010<1066:OSOTTU>2.0.CO;2.

Krishnamurti, T. N., and H. N. Bhalme, 1976: Oscillations of a monsoon system. Part I. Observational aspects. *J. Atmos. Sci.*, **33 (10)**, 1937–1954, doi:10.1175/1520-0469(1976)033<1937:OOAMSP>2.0.CO;2.

Kundu, P. K., I. M. Cohen, and D. R. Dowling, 2016: *Fluid Mechanics*. 6th ed., Academic Press, 921 pp.

Lenters, J. D., and K. H. Cook, 1997: On the origin of the Bolivian High and related circulation features of the South American climate. *J. Atmos. Sci.*, **54 (5)**, 656–678, doi:10.1175/1520-0469(1997)054<0656:OTOOTB>2.0.CO;2.

Lorensen, W. E., and H. E. Cline, 1987: Marching cubes: A high resolution 3D surface construction algorithm. *SIGGRAPH Comput. Graphics*, **21 (4)**, 163–169, doi:10.1145/37402.37422.

Luo, J., and Coauthors, 2018: Space–time variability in UTLS chemical distribution in the Asian summer monsoon viewed by limb and nadir satellite sensors. *Atmos. Chem. Phys.*, **18 (16)**, 12 511–12 530, doi:10.5194/acp-18-12511-2018.

MacVean, M. K., 1983: The effects of horizontal diffusion on baroclinic development in a spectral model. *Quart. J. Roy. Meteor. Soc.*, **109 (462)**, 771–783, doi:10.1002/qj.49710946206.

Madrid, J. A. J., and A. M. Mancho, 2009: Distinguished trajectories in time dependent vector fields. *Chaos*, **19 (1)**, 013 111, doi:10.1063/1.3056050.

Mantz, H., K. Jacobs, and K. Mecke, 2008: Utilizing Minkowski functionals for image analysis: A marching square algorithm. *J. Stat. Mech.: Theory Exp.*, **2008 (12)**, P12 015, doi:10.1088/1742-5468/2008/12/P12015.

Mason, R. B., and C. E. Anderson, 1963: The development and decay of the 100-mb. summertime anticyclone over Southern Asia. *Mon. Wea. Rev.*, **91 (1)**, 3–12, doi:10.1175/1520-0493(1963)091<0003:TDADOT>2.3.CO;2.

Matsuno, T., 1966: Quasi-geostrophic motions in the equatorial area. *J. Meteor. Soc. Japan*, **44 (1)**, 25–43, doi:10.2151/jmsj1965.44.1_25.

Neale, R. B., and Coauthors, 2012: Description of the NCAR Community Atmosphere Model (CAM 5.0). Tech. Rep. NCAR/TN-486+STR, National Center for Atmospheric Research, 274 pp.

Nützel, M., M. Dameris, and H. Garny, 2016: Movement, drivers and bimodality of the South Asian High. *Atmos. Chem. Phys.*, **16 (22)**, 14 755–14 774, doi:10.5194/acp-16-14755-2016.

Pan, L. L., S. B. Honomichl, D. E. Kinnison, M. Abalos, W. J. Randel, J. W. Bergman, and J. Bian, 2016: Transport of chemical tracers from the boundary layer to stratosphere associated with the dynamics of the Asian summer monsoon. *J. Geophys. Res. Atmos.*, **121 (23)**, 14 159–14 174, doi:10.1002/2016JD025616.

Phlips, P. J., and A. E. Gill, 1987: An analytic model of the heat-induced tropical circulation in the presence of a mean wind. *Quart. J. Roy. Meteor. Soc.*, **113 (475)**, 213–236, doi:10.1002/qj.49711347513.

Ploeger, F., and Coauthors, 2015: A potential vorticity-based determination of the transport barrier in the Asian summer monsoon anticyclone. *Atmos. Chem. Phys.*, **15 (22)**, 13 145–13 159, doi:10.5194/acp-15-13145-2015.

Popovic, J. M., and R. A. Plumb, 2001: Eddy shedding from the upper-tropospheric Asian monsoon anticyclone. *J. Atmos. Sci.*, **58 (1)**, 93–104, doi:10.1175/1520-0469(2001)058<0093:ESFTUT> 2.0.CO;2.

Rajon, D., and W. Bolch, 2003: Marching cube algorithm: Review and trilinear interpolation adaptation for image-based dosimetric models. *Comput. Med. Imaging Graphics*, **27 (5)**, 411 – 435, doi:10.1016/S0895-6111(03)00032-6.

Randel, W. J., and E. J. Jensen, 2013: Physical processes in the tropical tropopause layer and their roles in a changing climate. *Nat. Geosci.*, **6**, 169–176, doi:10.1038/ngeo1733.

Randel, W. J., and M. Park, 2006: Deep convective influence on the Asian summer monsoon anticyclone and associated tracer variability observed with Atmospheric Infrared Sounder (AIRS). *J. Geophys. Res. Atmos.*, **111 (D12)**, D12 314, doi:10.1029/2005JD006490.

Rangarajan, S., 1963: Thermal effects of the Tibetan Plateau during the Asian monsoon season. *Aust. Meteor. Mag.*, **42**, 24–34.

Santee, M. L., G. L. Manney, N. J. Livesey, M. J. Schwartz, J. L. Neu, and W. G. Read, 2017: A comprehensive overview of the climatological composition of the Asian summer monsoon anticyclone based on 10 years of Aura Microwave Limb Sounder measurements. *J. Geophys. Res. Atmos.*, **122 (10)**, 5491–5514, doi:10.1002/2016JD026408.

Schneider, T., 2004: The tropopause and the thermal stratification in the extratropics of a dry atmosphere. *J. Atmos. Sci.*, **61 (12)**, 1317–1340, doi:10.1175/1520-0469(2004)061<1317:TTATTS> 2.0.CO;2.

Schneider, T., and S. Bordoni, 2008: Eddy-mediated regime transitions in the seasonal cycle of a Hadley circulation and implications for monsoon dynamics. *J. Atmos. Sci.*, **65 (3)**, 915–934, doi:10.1175/2007JAS2415.1.

Schneider, T., and C. C. Walker, 2006: Self-organization of atmospheric macroturbulence into critical states of weak nonlinear eddy–eddy interactions. *J. Atmos. Sci.*, **63 (6)**, 1569–1586, doi:10.1175/JAS3699.1.

Schumacher, C., R. A. Houze Jr., and I. Kraucunas, 2004: The tropical dynamical response to latent heating estimates eerived from the TRMM precipitation radar. *J. Atmos. Sci.*, **61 (12)**, 1341–1358, doi:10.1175/1520-0469(2004)061<1341:TTDRTL>2.0.CO;2.

Siu, L. W., and K. P. Bowman, 2019: Forcing of the upper-tropospheric monsoon anticyclones. *J. Atmos. Sci.*, **76 (7)**, 1937–1954, doi:10.1175/JAS-D-18-0340.1.

Stensrud, D. J., 2013: Upscale effects of deep convection during the North American monsoon. *J. Atmos. Sci.*, **70 (9)**, 2681–2695, doi:10.1175/JAS-D-13-063.1.

Tandon, N. F., E. P. Gerber, A. H. Sobel, and L. M. Polvani, 2013: Understanding Hadley cell expansion versus contraction: Insights from simplified models and implications for recent observations. *J. Climate*, **26 (12)**, 4304–4321, doi:10.1175/JCLI-D-12-00598.1.

Tandon, N. F., L. M. Polvani, and S. M. Davis, 2011: The response of the tropospheric circulation to water vapor-like forcings in the stratosphere. *J. Climate*, **24 (21)**, 5713–5720, doi:10.1175/JCLI-D-11-00069.1.

Taschetto, A. S., R. J. Haarsma, A. S. Gupta, C. C. Ummenhofer, K. J. Hill, and M. H. England, 2010: Australian monsoon variability driven by a Gill–Matsuno-type response to central west Pacific warming. *J. Climate*, **23 (18)**, 4717–4736, doi:10.1175/2010JCLI3474.1.

TRMM, 2011: TRMM (TMPA) rainfall estimate L3 3 hour 0.25° × 0.25°, version 7. Goddard Earth Sciences Data and Information Services Center, accessed 1 January 2017, https://doi.org/10.5067/TRMM/TMPA/3H/7.

Ungermann, J., M. Ern, M. Kaufmann, R. Müller, R. Spang, F. Ploeger, B. Vogel, and M. Riese, 2016: Observations of PAN and its confinement in the Asian summer monsoon anticyclone in high spatial resolution. *Atmos. Chem. Phys.*, **16 (13)**, 8389–8403, doi:10.5194/acp-16-8389-2016.

Vallis, G. K., 2017: *Atmospheric and Oceanic Fluid Dynamics: Fundamentals and Large-Scale Circulation*. 2nd ed., Cambridge University Press, 946 pp.

van Mieghem, J., 1956: International Geophysical Year 1957-58: Meteorological programme. *World Meteor. Organ. Bull.*, **5 (1)**, 2–9.

Vera, C., and Coauthors, 2006: Toward a unified view of the American monsoon systems. *J. Climate*, **19 (20)**, 4977–5000, doi:10.1175/JCLI3896.1.

Vernier, J.-P., and Coauthors, 2018: BATAL: The balloon measurement campaigns of the Asian tropopause aerosol layer. *Bull. Amer. Meteor. Soc.*, **99 (5)**, 955–973, doi:10.1175/BAMS-D-17-0014.1.

Vogel, B., and Coauthors, 2014: Fast transport from Southeast Asia boundary layer sources to northern Europe: Rapid uplift in typhoons and eastward eddy shedding of the Asian monsoon anticyclone. *Atmos. Chem. Phys.*, **14 (23)**, 12 745–12 762, doi:10.5194/acp-14-12745-2014.

Vogel, B., and Coauthors, 2016: Long-range transport pathways of tropospheric source gases originating in Asia into the northern lower stratosphere during the Asian monsoon season 2012. *Atmos. Chem. Phys.*, **16 (23)**, 15 301–15 325, doi:10.5194/acp-16-15301-2016.

Wang, X., and Coauthors, 2018: The simulation of stratospheric water vapor over the Asian summer monsoon in CESM1(WACCM) models. *J. Geophys. Res. Atmos.*, **123 (20)**, 11,377–11,391, doi:10.1029/2018JD028971.

Webster, P. J., 1972: Response of the tropical atmosphere to local, steady forcing. *Mon. Wea. Rev.*, **100 (7)**, 518–541, doi:10.1175/1520-0493(1972)100<0518:ROTTAT>2.3.CO;2.

Webster, P. J., and J. R. Holton, 1982: Cross-equatorial response to middle-latitude forcing in a zonally varying basic state. *J. Atmos. Sci.*, **39 (4)**, 722–733, doi:10.1175/1520-0469(1982)039<0722:CERTML>2.0.CO;2.

Wei, W., R. Zhang, M. Wen, X. Rong, and T. Li, 2014: Impact of Indian summer monsoon on the South Asian High and its influence on summer rainfall over China. *Climate Dyn.*, **43 (5)**, 1257–1269, doi:10.1007/s00382-013-1938-y.

Wiggins, S., 1992: *Chaotic Transport in Dynamical Systems*. Springer-Verlag, New York, 301 pp.

Yanai, M., S. Esbensen, and J.-H. Chu, 1973: Determination of bulk properties of tropical cloud clusters from large-scale heat and moisture budgets. *J. Atmos. Sci.*, **30 (4)**, 611–627, doi:10.1175/1520-0469(1973)030<0611:DOBPOT>2.0.CO;2.

Zarrin, A., H. Ghaemi, M. Azadi, and M. Farajzadeh, 2010: The spatial pattern of summertime subtropical anticyclones over Asia and Africa: A climatological review. *Int. J. Climatol.*, **30 (2)**, 159–173, doi:10.1002/joc.1879.

Zhang, Q., G. Wu, and Y. Qian, 2002: The bimodality of the 100 hPa South Asia High and its relationship to the climate anomaly over East Asia in summer. *J. Meteor. Soc. Japan*, **80 (4)**, 733–744, doi:10.2151/jmsj.80.733.